Fluvial bar instability with bank erosion

by

Md Jahir Uddin

A thesis submitted in partial fulfillment of the requirements for the degree of
Doctor of Engineering

Examination Committee: Prof. Norihiro Izumi
Prof. Yasuyuki Shimizu
Prof. Toshihiko Yamashita
Assoc. Prof. Tomihito Yamada

Doctoral Thesis No. EG-M...
Division of Field Engineering for the Environment
Graduate School of Engineering, Hokkaido University
March 2015

Acknowledgment

I would like to take this change to express my sincere gratitude to my supervisor, Professor Norihiro Izumi, for his patience, guidance and help for my study and life in Japan. And in my study periods, I have learn from Izumi sensei both knowledge and thinking methods. Sensei teaches me how to behave methodically and logically for a complicated task with optimistic attitude. And I believe that this will benefit me for a life time. Sensei sets a good example for me to learn. In fact, I imitate Sensei's behaviors unconsciously.

I want to extend special thanks to Associate Professor Tomihito Yamada Sensei. During my research, Sensei always provides me valuable suggestions which help me to improve my study.

I am very grateful all of my laboratory members, for their instant help for my laboratory life.

Thanks for my family members who are always behind me and encourage for this study periods.

At last I want to say, it has been a great experience to study in Hokkaido University. I enjoy the beautiful campus and love the nice people here.

Abstract

Linear stability analysis of fluvial sand bars involving bank erosion is performed with the use of the shallow-water equations, the Exner equation, and the bank erosion equation newly proposed in this study. For performing linear stability analysis, it is considered flow in channels with erodible banks and beds. This study assumed that the length scales of bar formation and bank erosion in the streamwise direction are on the same order of magnitude in the range of linear stability analysis. In this study, the quasi-steady assumption has been employed in which time scale of flow variation is sufficiently short compared with that of topographical variations of bed and banks, and therefore, the flow can be assumed to achieve equilibrium state immediately and the time derivative terms in the flow equations can be dropped.

This study employs simple assumptions of bank erosion processes that the location of banks are shifted over time with the average channel width kept constant but the local channel width itself can change in space and time. In addition to the boundary condition of flow, additional boundary conditions of sediment continuity at the banks are imposed for the solution of all the equations. It is assumed that the river bed and banks are composed of gravel and bank erosion takes place due to increases in the bed shear stress in the vicinity of banks. If the bed shear stress at the junction between the laterally sloped bank region and the horizontally flat central bed region increases, sediment on the bank region starts to move. Once sediment starts to move on the bank region, sediment is removed from the bank because it is pulled in the lateral direction by the gravity. This results in bank erosion. It is assumed, therefore, that the bank erosion speed depends on how large the bed shear stress at the junction is compared with some critical bed shear stress.

The shallow water equations are analyzed with perturbation techniques. The resulting perturbation equation is solved by the boundary conditions with the use of the spectral collocation method with the Chebyshev polynomials. The analysis provides the growth rate of perturbation as a function of the wavenumber, the aspect ratio, and the bank erodibility. Instability diagram is obtained from this numerical solution, and find the contours of the maximum growth rate corresponding to multiple bars with a variety of modes (lateral wavenumbers) as well as single alternate bars. The awkward shapes of contours are also found in the diagram

which are caused by the superposition of a number of contours of single alternate bars and multiple bars with different modes. It is found that the flat bed becomes unstable in a wider range of wavenumber with increasing the value of bank erosion coefficient γ. This implies that the bed instability is intensified by bank erosion.

Analytical solutions are also obtained by the use of asymptotic expansions around the state of no bank erosion (the bank erosion coefficient γ equals 0) in order to clarify the effect of bank erosion on the instability of sand bars with different lateral wavenumbers. Because γ is a bank erosion coefficient, the problem reduces to the original bar instability problem at the lowest order of γ. The bank erosion coefficient γ has been evaluated from field data (ranges 4.27×10^{-5} to 4.39×10^{-2}) and experimental data (0.5).

From the analytical solution, instability diagram is obtained, and found that bank erosion stabilizes the bed in the ranges of small wavenumbers, and of large wavenumbers and aspect ratios. It was found from the analysis that the tendency of expanded unstable region is remarkable especially in the case of single alternate bars. The expansion of unstable region in the direction of increasing wavenumbers means that the wavelength of bars decreases. The implication is that excessive sediment supplied due to bank erosion causes the increase of bed instability, and the resulting decrease in the bar wavelength. It is also found that if the value of γ is smaller than 0.04, the effect of bank erosion is negligible at least in the instability diagram.

From the instability diagram, the discontinuous changes of neutral curves in the ranges of large aspect ratios and wavenumbers have been found. It is also found that the discontinuity is not observed in the case of large Froude numbers. From these results, it is suspected that the term at $O(\gamma)$ becomes too large for the expansion to be valid. The analytical solution is assumed to be applicable only in the ranges of relatively small aspect ratios and wavenumbers, and large Froude numbers.

The analytical solution and numerical solution have been compared, and found from the instability diagram that the envelope of all the neutral curves of analytical solution agrees well with the neutral curve of numerical solution in the range of large wavenumbers. It is found, however, the agreement is not good in the range of small wavenumbers.

The bed topography obtained from the present analysis has been compared with

that obtained in the Watanabe's experiments (2015). The similar pattern of bed topography has been found from the comparisons. The wavelength of bars predicted by the present analysis has also been compared with field data. Only field data of meandering is selected with significant bars. The prediction obtained in the present analysis agree better with the field data than that obtained in the analysis of meandering performed by Ikeda et al. (1981). This implies that the some cases of meandering can possibly be explained by the present theory of the bar instability with bank erosion. The present analysis is also tested with the use of experimental data obtained by Watanabe, Corasato and Hasegawa. A reasonable agreement can be seen between the prediction and the experimental data.

Contents

List of Figures

List of Tables

Chapter 1

Introduction

Fluvial bars are one of the characteristic morphological features observed in rivers. Bars can be classified as free and forced as relating to their origin. According to Seminara and Tubino (1989), free bars spontaneously develop because of an instability of the flow bed system. Callander (1969) descrided that single row alternate bars are the familiar type of free bars in sandy streams and gravel bed rivers when the channel is narrow enough. In the case of a channel that represents large width to depth aspect ratio, the rivers grow multiple bars leading to braiding patterns, (Fujita and Muramoto (1985); Crosato and Mosselman (2009)). Fluvial bars may also be forced (called forced bar) by various effects like curvature, variations of channel width or confluences etc.

There have been a number of analytical studies on fluvial bars, but they are assuming straight fixed banks. Since the first analytical study on the formation of bars in terms of linear stability analysis performed by Callander (1969), a great number of analytical studies have been conducted by researchers in the fields of not only civil engineering also geophysics and mathematics. It can also be said that analytical study has been well developed by weakly non-linear stability analysis of Colombini *et al.* (1987). They studied to determine the development of finite-amplitude alternate bars in straight channels with erodible bottoms, and consider the flow in a straight channel with constant width and non-erodible banks. The result of their two-timescale analysis was a so-called Landau-Stuart equation describing the time evolution of the wave amplitude. They also derived that all non-transient solutions of this equation are periodic and signify a finite-amplitude periodic alternate bar

Figure 1.1: The satellite image of the Jamuna River. From Google Earth.

pattern.

There is only one study on bars with sinuous fixed banks by Fu-Chun and Tzu-Hao (2005), but it can shed no light on the interaction between bars and bank erosion that should exist in nature. They have studied the forced bars induced by variation of channel width. Their investigation makes clear conditions under which different types of forced bars may form in channels with periodic width variations. They used a depth average two-dimensional model incorporating a simplified correction for helical flows induced by stream line curvature to obtain analytical solution of bed deformation, and verify the model results with flume experiment. Their analytical solution is used to obtain a criterion for central bar formation, which implies a condition necessary for incipient bifurcation. In terms of the relation between river bank geometry and river bed topography in nature, however, not only the former affects the latter, also the latter affects the former. There should be a mutual interaction between river bank geometry and river bed topography.

Figure 1.1 is the satellite image of the Jamuna river in Bangladesh which is

known as a typical river characterized by multiple bars and braided channels. As seen in the figure, the formation of bars are accompanied by periodic geometry of the channel width. This suggests that the variation of the channel width and the channel geometry may have important influences on the bar instability.

In this study, we perform linear stability analysis of sand fluvial bars with bank erosion incorporated. We obtain numerical solution from the resulting perturbation equations involved in the linear stability analysis. In order to clarify the effect of bank erosion on the instability of sand bars, we also obtain analytical solution by the use of asymptotic expansions around the state of no bank erosion in which the bank erosion coefficient γ vanishes. Because γ is a coefficient representing bank erosion coefficient, the problem reduces to the original bar instability problem at the lowest order of γ. We have evaluated γ from field and experimental data to see the effects of bank erosion on bar instability. We have compared the numerical solutions with analytical solutions to observe the validity limit of the γ expansion. We also compare the bed topography obtained from our analysis with that obtained in the Watanabe's experiments (2015). The wavelength of bars predicted by our analysis has been compared with selected field data of meandering with significant bars. We also test our analysis with the use of experimental data obtained by Watanabe, Corasato and Hasegawa.

Chapter 2

Formulation

2.1 Governing equations

In this thesis, we study the linear stability of erodible banks as well as beds to small disturbances. We consider flow in the channel with sinuous bank as shown in Fig. 2.1. We assume that the length scales of bar formation and bank erosion in the streamwise direction are on the same order of magnitude in the region of linear stability analysis. It is, then, expected that the flow can be described by the shallow water equations of the form

$$\tilde{U}\frac{\partial \tilde{U}}{\partial \tilde{x}} + \tilde{V}\frac{\partial \tilde{U}}{\partial \tilde{y}} = -g\frac{\partial \tilde{H}}{\partial \tilde{x}} - g\frac{\partial \tilde{Z}}{\partial \tilde{x}} - \frac{\tilde{T}_{bx}}{\rho \tilde{H}} \tag{2.1}$$

$$\tilde{U}\frac{\partial \tilde{V}}{\partial \tilde{x}} + \tilde{V}\frac{\partial \tilde{V}}{\partial \tilde{y}} = -g\frac{\partial \tilde{H}}{\partial \tilde{y}} - g\frac{\partial \tilde{Z}}{\partial \tilde{y}} - \frac{\tilde{T}_{by}}{\rho \tilde{H}} \tag{2.2}$$

$$\frac{\partial \tilde{U}\tilde{H}}{\partial \tilde{x}} + \frac{\partial \tilde{V}\tilde{H}}{\partial \tilde{y}} = 0 \tag{2.3}$$

where $\tilde{x}$ and $\tilde{y}$ are the streamwise and lateral coordinates respectively, $\tilde{U}$ and $\tilde{V}$ are the $\tilde{x}$ and $\tilde{y}$ components of the flow velocity respectively, $\tilde{H}$ and $\tilde{Z}$ are the flow depth and bed elevation respectively, and $\tilde{T}_{bx}$ and $\tilde{T}_{by}$ are the $\tilde{x}$ and $\tilde{y}$ components of the bed shear stress respectively. The tilde is used to indicate dimensional variables hereafter. In the above equations, we have employed the quasi-steady assumption in which time scale of flow variation is sufficiently short compared with that of topographical variations of bed and banks, and therefore, the flow can be assumed to achieve equilibrium state immediately and the time derivative terms in the flow

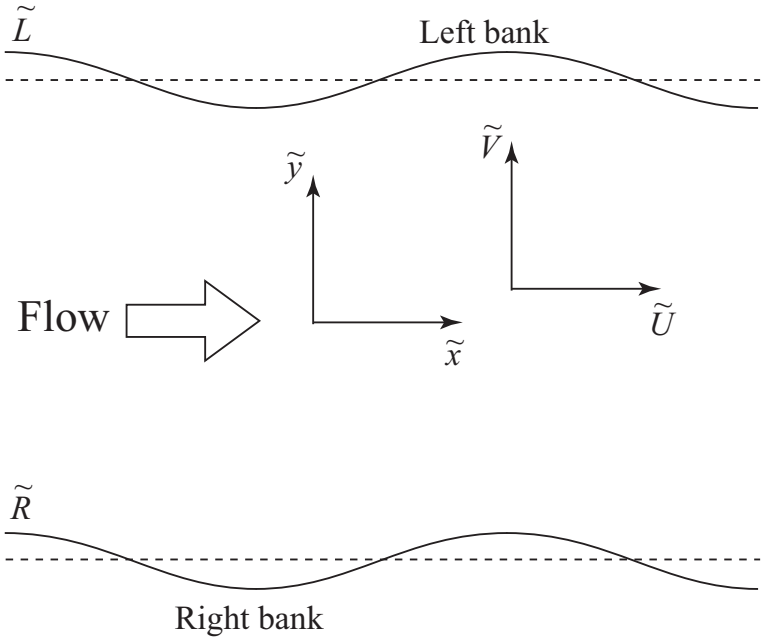

Figure 2.1: Conceptual diagram and coordinates for left and right banks being in phase.

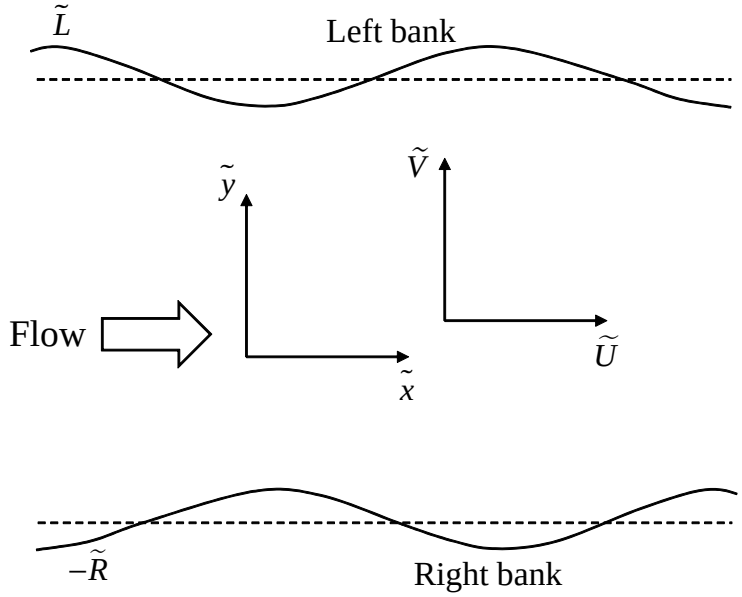

Figure 2.2: Conceptual diagram and coordinates for left and right banks being out of phase.

equations can be dropped. We assume that the x and y components of the bed shear stress, $\tilde{T}_{bx}$ and $\tilde{T}_{by}$, take the form

$$\left(\tilde{T}_{bx}, \tilde{T}_{by}\right) = \tilde{T}_b \left(\tilde{U}, \tilde{V}\right) \left(\tilde{U}^2 + \tilde{V}^2\right)^{-1/2} \tag{2.4}$$

where $\tilde{T}_b$ is the total bed shear stress, written in the form

$$\tilde{T}_b = \rho C_f \left(\tilde{U}^2 + \tilde{V}^2\right) \tag{2.5}$$

with C_f being the bed friction coefficient, which is known to be a week function of the flow depth relative to the roughness height. However, it is assumed to be a constant for simplicity herein and can be estimated from Keulegan (1938) formula

$$C_f = \left(6 + 2.5 \ln \frac{\tilde{H}_n}{k_s}\right)^{-2} \tag{2.6}$$

in which k_s is roughness height set equal to 2.5 $\tilde{d}_s$ after Engelund and Hansen (1967). ρ is the water density.

The time variation of the bed elevation is described by

$$(1 - \lambda_p) \frac{\partial \tilde{Z}}{\partial \tilde{t}} + \frac{\partial \tilde{Q}_{bx}}{\partial \tilde{x}} + \frac{\partial \tilde{Q}_{by}}{\partial \tilde{y}} = 0 \tag{2.7}$$

where λ_p is porosity, and $\tilde{Q}_{bx}$ and $\tilde{Q}_{by}$ are the $\tilde{x}$ and $\tilde{y}$ components of bedload sediment transport rate respectively, which are expressed by the use of the angle between the direction of bedload and the $\tilde{x}$ axis, ϕ, such that

$$\left(\tilde{Q}_{bx}, \tilde{Q}_{by}\right) = \tilde{Q}_b \left(\cos\phi, \sin\phi\right) \tag{2.8}$$

In the above equation $\tilde{Q}_b$ is the total bedload rate, which is assumed to be described by the Meyer-Peter and Müller formula, in the form given by Chien (1954) such that

$$\tilde{Q}_b = 8 \left(\theta - \theta_c\right)^{3/2} \left(R_s g \tilde{d}_s^3\right)^{1/2} \tag{2.9}$$

where θ is the non-dimensional bed shear stress, θ_c is the non-dimensional critical bed shear stress, which is assumed to be a constant of 0.047, R_s is the submerged

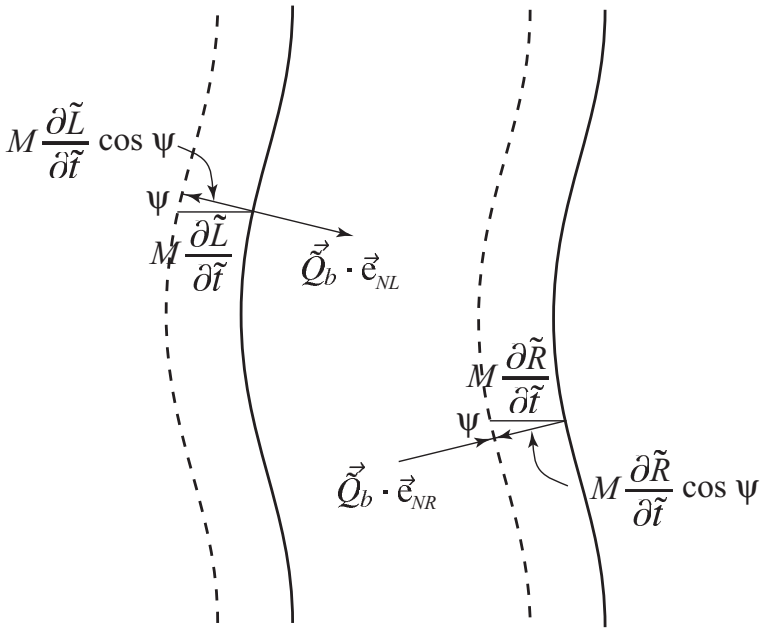

Figure 2.3: The boundary condition of sediment flux at banks.

specific gravity, which is assumed to take a standard value of 1.65, g is gravitational acceleration (= 9.8 m/s^2), and $\tilde{d}_s$ is the sediment diameter. The non-dimensional bed shear stress is defined by

$$\theta = \frac{\tilde{T}_b}{\rho R_s g \tilde{d}_s} \tag{2.10}$$

The sine of the direction angle of bedload, $\sin\phi$, is expressed by the following formula derive by Engelund (1981)

$$\sin\phi = \frac{\tilde{V}}{\left(\tilde{U}^2 + \tilde{V}^2\right)^{1/2}} - \frac{r}{\theta^{1/2}} \frac{\partial \tilde{Z}}{\partial \tilde{y}} \tag{2.11}$$

where r is a coefficient (probably dependent on the particle Reynolds number) which various authors suggest to take as a constant ranging between 0.3 by Olesen (1983) and 0.6 by Engelund (1981). In our study we use $r = 0.3$.

2.2 Boundary conditions

We assume that the locations of banks are shifted over time. Figures 2.1 and 2.2 show the conceptual diagram and coordinates system employed in this analysis. Denoting the $\tilde{y}$ coordinates of right and left banks by $\tilde{R}$ and $\tilde{L}$ respectively, and the

total channel width by $\tilde{B}$, we obtain the relation

$$\tilde{B} = \tilde{L} - \tilde{R} \tag{2.12}$$

where we assume that the average value of total channel width $\tilde{B}$ is constant, but local channel width itself can change in space and time.

The flow cannot penetrate the both banks, so that the velocity components normal to the both banks should vanish, such that

$$\tilde{\boldsymbol{U}} \cdot \boldsymbol{e}_{NR} = 0 \quad \text{at} \quad \tilde{y} = \tilde{R} \tag{2.13}$$

$$\tilde{\boldsymbol{U}} \cdot \boldsymbol{e}_{NL} = 0 \quad \text{at} \quad \tilde{y} = \tilde{L} \tag{2.14}$$

where the quasi-steady assumption has been employed as well as in the shallow water equations. In the above equation, $\tilde{\boldsymbol{U}}$ is the velocity vector, defined by

$$\tilde{\boldsymbol{U}} = \left(\tilde{U}, \tilde{V}\right) \tag{2.15}$$

In addition, $\boldsymbol{e}_{NL}$ and $\boldsymbol{e}_{NR}$ are unit vectors normal to the left and right banks respectively, expressed by

$$\boldsymbol{e}_{NL} = \frac{(-\partial\tilde{L}/\partial\tilde{x}, 1)}{\sqrt{1 + (\partial\tilde{L}/\partial\tilde{x})^2}} \tag{2.16}$$

$$\boldsymbol{e}_{NR} = \frac{(-\partial\tilde{R}/\partial\tilde{x}, 1)}{\sqrt{1 + (\partial\tilde{R}/\partial\tilde{x})^2}} \tag{2.17}$$

Figure 2.3 shows the boundary condition of sediment flux at banks, where the solid thick lines indicate the original bank line and broken lines denote the bank line after erosion or deposition. Bank erosion produces sediment supply from the banks to the channel. When the time variation of $\tilde{R}$ is positive, the deposition takes place on the right bank. Therefore, the sediment is absorbed by the right bank, and the negative sediment supply takes place on the right bank. That process is formulated by

$$\left[\tilde{M} - \left(\tilde{Z} + S\tilde{x}\right)\right] \frac{\partial\tilde{R}}{\partial\tilde{t}} \cos\psi = -\tilde{\boldsymbol{Q}}_b(\tilde{R}) \cdot \boldsymbol{e}_{NR} \tag{2.18}$$

where $\tilde{M}$ is the bank height, and $\tilde{Z} + S\tilde{x}$ is the deviation of the bed elevation from the original plane bed, and S is the bed slope. Therefore, the relative variation

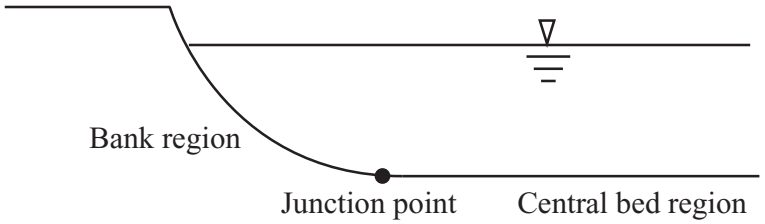

Figure 2.4: Channel cross-section.

of bank height due to the bed degradation in the vicinity of the bank is taken into account in the above equation. Meanwhile, when the time variation of $\tilde{L}$ is negative, the erosion takes place on the left bank. Therefore, the sediment is added to the river from the left bank, and the positive sediment supply takes place on the left bank. So the process can be formulated by

$$\left[\tilde{M} - \left(\tilde{Z} + S\tilde{x}\right)\right] \frac{\partial \tilde{L}}{\partial \tilde{t}} \cos\psi = -\tilde{\boldsymbol{Q}}_b(\tilde{L}) \cdot \boldsymbol{e}_{NL} \tag{2.19}$$

where ψ is the angle between the bank and the $\tilde{y}$ axis, and $\tilde{\boldsymbol{Q}}_b$ is the bedload vector, described by

$$\tilde{\boldsymbol{Q}}_b = \left(\tilde{Q}_{bx}, \tilde{Q}_{by}\right) \tag{2.20}$$

2.3 Bank erosion model

Bank erosion can take place from a variety of mechanisms in which lots of factors play a role. It can be a result of discharge-induced flow and sediment transport, but also of processes beyond the basic system of river morphology. Ikeda *et al.* (1981) provide a model in which the bank erosion rate is proportional to the excess flow velocity above a certain critical value. They take this critical value to be equal to the reach-averaged flow velocity. In this study, we assume that the river bed and banks are composed of gravel and that bank erosion takes place due to increases in the bed shear stress in the vicinity of banks. If the bed shear stress at the junction between the laterally sloped bank region and the horizontally flat central bed region increases, sediment on the bank region starts to move (see Fig. 2.4), Parker (1978b); Ikeda and Izumi (1990). Once sediment starts to move on the bank region, sediment is removed from the bank because it is pulled in the lateral direction by the gravity.

This results in bank erosion. It is assumed, therefore, that the bank erosion speed depends on how large the bed shear stress at the junction is compared with the critical bed shear stress. We employ a simple relation of the form

$$-\left[\tilde{M}-\left(\tilde{Z}+S\tilde{x}\right)\right]\frac{\partial\tilde{R}}{\partial t}\cos\psi=\tilde{\gamma}\left[\theta(\tilde{R})-\theta_n\right]\quad\text{at}\quad\tilde{y}=\tilde{R}\tag{2.21}$$

$$\left[\tilde{M}-\left(\tilde{Z}+S\tilde{x}\right)\right]\frac{\partial\tilde{L}}{\partial t}\cos\psi=\tilde{\gamma}\left[\theta(\tilde{L})-\theta_n\right]\quad\text{at}\quad\tilde{y}=\tilde{L}\tag{2.22}$$

where θ_n is the non-dimensional bed shear stress in the base state flat bed condition before bars are formed, and is known to be approximately 1.2 times larger than the critical bed shear stress for bedload motion in the case of gravel bed rivers. In addition, $\tilde{\gamma}$ is an empirical constant with the dimension of sediment transport rate, representing the bank erosion coefficient.

2.4 Normalization

The following normalization is employed

$$\left(\tilde{x},\tilde{y},\tilde{B},\tilde{L},\tilde{R}\right)=\tilde{B}_n\left(x,y,B,L,R\right)\tag{2.23a}$$

$$\left(\tilde{U},\tilde{V}\right)=\tilde{U}_n\left(U,V\right),\quad\left(\tilde{H},\tilde{Z}\right)=\tilde{H}_n\left(H,Z\right)\tag{2.23b, c}$$

$$\left(\tilde{Q}_b,\tilde{Q}_{bx},\tilde{Q}_{by}\right)=\sqrt{R_sg\tilde{d}_s^3}\left(Q_b,Q_{bx},Q_{by}\right),\quad\tilde{t}=\frac{(1-\lambda_p)\tilde{H}_n\tilde{B}_n}{\sqrt{R_sg\tilde{d}_s^3}}t\tag{2.23d, e}$$

Here $\tilde{B}_n$, $\tilde{U}_n$ and $\tilde{H}_n$ are the channel width, flow velocity, and flow depth in the base state flat bed condition. With the use of the above normalization, the governing equation (2.1)–(2.3), (2.7)–(2.9) and (2.11) are rewritten in the form

$$U\frac{\partial U}{\partial x}+V\frac{\partial U}{\partial y}+F^{-2}\left(\frac{\partial H}{\partial x}+\frac{\partial Z}{\partial x}\right)+\beta C_f\frac{\left(U^2+V^2\right)^{1/2}U}{H}=0\tag{2.24}$$

$$U\frac{\partial V}{\partial x}+V\frac{\partial V}{\partial y}+F^{-2}\left(\frac{\partial H}{\partial y}+\frac{\partial Z}{\partial y}\right)+\beta C_f\frac{\left(U^2+V^2\right)^{1/2}V}{H}=0\tag{2.25}$$

$$\frac{\partial UH}{\partial x}+\frac{\partial VH}{\partial y}=0\tag{2.26}$$

$$\frac{\partial Z}{\partial t} + \frac{\partial Q_{bx}}{\partial x} + \frac{\partial Q_{by}}{\partial y} = 0 \tag{2.27}$$

$$(Q_{bx}, Q_{by}) = Q_b \left(\cos\phi, \sin\phi\right) \tag{2.28}$$

$$Q_b = 8\left(\theta - \theta_c\right)^{3/2}, \quad \sin\phi = \frac{V}{\sqrt{U^2+V^2}} - \frac{r}{\beta\theta^{1/2}}\frac{\partial Z}{\partial y} \tag{2.29a, b}$$

where β is the aspect ratio defined as the ratio between the channel width and flow depth at the base state flat bed condition, and F is the unperturbed Froude number. It might be worth while to point out that the non-dimensional bed shear stress in the above equation θ can be described by

$$\theta = \theta_n \left(U^2 + V^2\right) \tag{2.30}$$

where θ_n is the non-dimensional bed shear stress in the base state flat bed condition, which is sometimes called the Shields number.

The boundary conditions (2.13), (2.14), (2.18), (2.19), (2.21) and (2.22) are normalized to be

$$\boldsymbol{U} \cdot \boldsymbol{e}_{NR} = 0 \quad \text{at} \quad y = R \tag{2.31}$$

$$\boldsymbol{U} \cdot \boldsymbol{e}_{NL} = 0 \quad \text{at} \quad y = L \tag{2.32}$$

$$\left(M - Z - \beta C_f F^2 x\right)\frac{\partial R}{\partial t}\cos\psi = -\boldsymbol{Q}_b(R) \cdot \boldsymbol{e}_{NR} \quad \text{at} \quad y = R \tag{2.33}$$

$$\left(M - Z - \beta C_f F^2 x\right)\frac{\partial L}{\partial t}\cos\psi = -\boldsymbol{Q}_b(L) \cdot \boldsymbol{e}_{NL} \quad \text{at} \quad y = L \tag{2.34}$$

$$\left(M - Z - \beta C_f F^2 x\right)\frac{\partial R}{\partial t}\cos\psi = -\gamma\left[\theta(R) - \theta_n\right] \quad \text{at} \quad y = R \tag{2.35}$$

$$\left(M - Z - \beta C_f F^2 x\right)\frac{\partial L}{\partial t}\cos\psi = \gamma\left[\theta(L) - \theta_n\right] \quad \text{at} \quad y = L \tag{2.36}$$

where

$$\gamma = \frac{\tilde{\gamma}}{\sqrt{R_s g \tilde{d}_s^3}}, \quad M = \frac{\tilde{M}}{\tilde{H}_n} \tag{2.37a, b}$$

Chapter 3

Linear stability analysis

3.1 Asymptotic expansions with A

We impose perturbation with a sinusoidal shape on the flow velocity, flow depth, and bed elevation. For performing linear stability analysis, we employ the asymptotic expansions of the form

$$U(x,y) = 1 + AU_1(y)\exp\left[\mathrm{i}(kx-\omega t)\right] \tag{3.1a}$$

$$V(x,y) = AV_1(y)\exp\left[\mathrm{i}(kx-\omega t)\right] \tag{3.1b}$$

$$H(x,y) = 1 + AH_1(y)\exp\left[\mathrm{i}(kx-\omega t)\right] \tag{3.1c}$$

$$Z(x,y,t) = -\beta C_f F^2 x + AZ_1(y)\exp\left[\mathrm{i}(kx-\omega t)\right] \tag{3.1d}$$

where A, k and ω are the amplitude, wavenumber and angular frequency of perturbation, respectively. At the same time as the above variables, the locations of the right and left banks $R(x,t)$ and $L(x,t)$ are expanded in the similar form

$$R(x,t) = -\frac{1}{2} + AR_1\exp\left[\mathrm{i}(kx-\omega t)\right] \tag{3.2a}$$

$$L(x,t) = \frac{1}{2} + AL_1\exp\left[\mathrm{i}(kx-\omega t)\right] \tag{3.2b}$$

Substituting the above expansions into (2.1)–(2.3) and (2.7), we obtain the following differential system at $O(A)$

$$(\mathrm{i}k + 2\beta C_f)\, U_1(y) + \left(\mathrm{i}kF^{-2} - \beta C_f\right) H_1(y) + \mathrm{i}kF^{-2} Z_1(y) = 0 \tag{3.3}$$

$$(\mathrm{i}k + \beta C_f)\, V_1(y) + F^{-2}\frac{\mathrm{d}H_1}{\mathrm{d}y} + F^{-2}\frac{\mathrm{d}Z_1}{\mathrm{d}y} = 0 \tag{3.4}$$

$$\mathrm{i}kU_1(y) + \frac{\mathrm{d}V_1}{\mathrm{d}y} + \mathrm{i}kH_1(y) = 0 \tag{3.5}$$

$$-\mathrm{i}\omega Z_1(y) + 24\mathrm{i}k\theta_n \left(\theta_n - \theta_c\right)^{1/2} U_1(y) + 8\left(\theta_n - \theta_c\right)^{3/2} \frac{\mathrm{d}V_1}{\mathrm{d}y} - \frac{8\left(\theta_n - \theta_c\right)^{3/2} r}{\beta\theta_n^{1/2}} \frac{\mathrm{d}^2 Z_1}{\mathrm{d}y^2} = 0 \tag{3.6}$$

Since the amplitude of the perturbation A is assumed to be infinitesimally small, the terms containing A^2 have been dropped in the linear stability analysis, so that the results of the analysis are valid only in the range of small amplitudes. The above perturbation equations are rewritten in the matrix form

$$\mathbf{L} \cdot \boldsymbol{U} = 0 \tag{3.7a}$$

where

$$\mathbf{L} = [L_{ij}], \quad \boldsymbol{U} = [U_1, V_1, H_1, Z_1]^T \tag{3.7b, c}$$

$$L_{11} = \mathrm{i}k + 2\beta C_f, \quad L_{21} = 0, \quad L_{31} = \mathrm{i}kF^{-2} - \beta C_f$$

$$L_{41} = \mathrm{i}kF^{-2}, \quad L_{12} = 0, \quad L_{22} = \mathrm{i}k + \beta C_f, \quad L_{32} = F^{-2}\frac{\mathrm{d}}{\mathrm{d}y}$$

$$L_{42} = F^{-2}\frac{\mathrm{d}}{\mathrm{d}y}, \quad L_{13} = \mathrm{i}k, \quad L_{23} = \frac{\mathrm{d}}{\mathrm{d}y}, \quad L_{33} = \mathrm{i}k,$$

$$L_{43} = 0, \quad L_{14} = 24\mathrm{i}k\theta_n \left(\theta_n - \theta_c\right)^{1/2}, \quad L_{24} = 0$$

$$L_{34} = 8\left(\theta_n - \theta_c\right)^{3/2} \frac{\mathrm{d}}{\mathrm{d}y}, \quad L_{44} = \frac{8r\left(\theta_n - \theta_c\right)^{3/2}}{\beta\theta_n^{1/2}} \frac{\mathrm{d}^2}{\mathrm{d}y^2} - \mathrm{i}\omega$$

Substituting (3.1)–(3.2) into (2.13), (2.14), (2.18), (2.19), (2.21) and (2.22), we obtain the following differential system at $O(A)$

$$-\mathrm{i}kR_1 + V_1\left(-\frac{1}{2}\right) = 0 \tag{3.8}$$

$$-\mathrm{i}kL_1 + V_1\left(\frac{1}{2}\right) = 0 \tag{3.9}$$

$$-\mathrm{i}\omega M R_1 - 8\mathrm{i}k\left(\theta_n - \theta_c\right)^{3/2} R_1 + 8\left(\theta_n - \theta_c\right)^{3/2} V_1\left(-\frac{1}{2}\right)$$
$$-\frac{8r\left(\theta_n - \theta_c\right)^{3/2}}{\beta\theta_n^{1/2}}\frac{\mathrm{d}Z_1\left(-\frac{1}{2}\right)}{\mathrm{d}y} = 0 \tag{3.10}$$

$$-\mathrm{i}\omega M L_1 - 8\mathrm{i}k\left(\theta_n - \theta_c\right)^{3/2} L_1 + 8\left(\theta_n - \theta_c\right)^{3/2} V_1\left(\frac{1}{2}\right)$$
$$-\frac{8r\left(\theta_n - \theta_c\right)^{3/2}}{\beta\theta_n^{1/2}}\frac{\mathrm{d}Z_1\left(\frac{1}{2}\right)}{\mathrm{d}y} = 0 \tag{3.11}$$

$$-\mathrm{i}\omega M R_1 + 2\gamma\theta_n U_1\left(-\frac{1}{2}\right) = 0 \tag{3.12}$$

$$-\mathrm{i}\omega M L_1 - 2\gamma\theta_n U_1\left(\frac{1}{2}\right) = 0 \tag{3.13}$$

Eliminating R_1 and L_1, the above boundary conditions reduce to

$$\frac{\omega}{k} M V_1\left(\pm\tfrac{1}{2}\right) = -\frac{8\left(\theta_n - \theta_c\right)^{3/2} r}{\beta\theta_n^{1/2}}\frac{\mathrm{d}Z_1\left(\pm\frac{1}{2}\right)}{\mathrm{d}y} \tag{3.14}$$

$$\frac{\omega}{k} M V_1\left(\pm\tfrac{1}{2}\right) = \mp 2\gamma\theta_n U_1\left(\pm\tfrac{1}{2}\right) \tag{3.15}$$

The equations (3.3)–(3.6) is an ordinary differential equations for four unknown variables U_1, V_1, H_1, Z_1, where U_1 is 0-order, V_1 and H_1 is 1-order, Z_1 is 2-order. Therefore, these are the 4th-order linear homogeneous ordinary differential equation. The boundary conditions (3.8)–(3.13) is also linear homogeneous equations including two more unknown of R_1 and L_1. Equations (3.3)–(3.6) and (3.8)–(3.13) constitute a linear eigenvalue problem that contains the eigenvalues ω. We have solved the above (3.3)–(3.6) 4th-order linear homogeneous ordinary differential equation by using the boundary conditions (3.14)–(3.15), first by numerically in section 3.2, and then by analytically in chapter 4.

3.2 Numerical solution

We have used a numerical scheme to solve the governing equations (3.3)–(3.6) under the boundary conditions (3.14)–(3.15). We employ a spectral collocation method with the Chebyshev polynomials. In the zone $-1/2 \leq y \leq 1/2$, the variables are expanded in the form

$$U_1(y) = \sum_{j=0}^{N} a_j T_j(\xi), \quad V_1(y) = \sum_{j=0}^{N} a_{(N+1)+j} T_j(\xi) \tag{3.16a, b}$$

$$H_1(y) = \sum_{j=0}^{N} a_{2(N+1)+j} T_j(\xi), \quad Z_1(y) = \sum_{j=0}^{N} a_{3(N+1)+j} T_j(\xi) \tag{3.16c, d}$$

where $a_j (j = 0, 1, 2, \cdots, 4N+3)$ are the coefficient of the Chebyshev polynomials, and $T_j(\xi)$ is the Chebyshev polynomials in ξ of degree j. The independent variables ξ range from -1 to 1, and is related to y by the equation $\xi = 2y$ $(-1/2 \leq y \leq 1/2)$. The expansion (3.16) substitute into the governing equations (3.3)–(3.6), and the resulting equations are evaluated at the Gauss-Lobatto points defined by

$$\xi_m = \frac{1}{2} cos \frac{m\pi}{N} \tag{3.17}$$

where $m = 0, 1, 2, \cdots, N$. Therefore, the number of points where the governing equations are evaluated is $N + 1$. We obtained a system of $4(N + 1)$ algebraic equations with $4(N + 1)$ unknown coefficient $a_0, a_1, a_2, \cdots, a_{4N+3}$. The equations of the system are then replaced by the four boundary conditions (3.14)–(3.15). The resulting linear algebraic system can be written in the form

$$\mathbf{L} \begin{bmatrix} a_0 \\ a_1 \\ \vdots \\ a_{4N+3} \end{bmatrix} = 0 \tag{3.18}$$

where $\mathbf{L}$ is a $4(N+1) \times 4(N+1)$ matrix in which the elements consist of the coefficients of U_1, V_1, H_1 and Z_1 in the governing equations (3.3)–(3.6) and the boundary conditions (3.14)–(3.15). The condition for (3.18) to have a non-trivial solution is

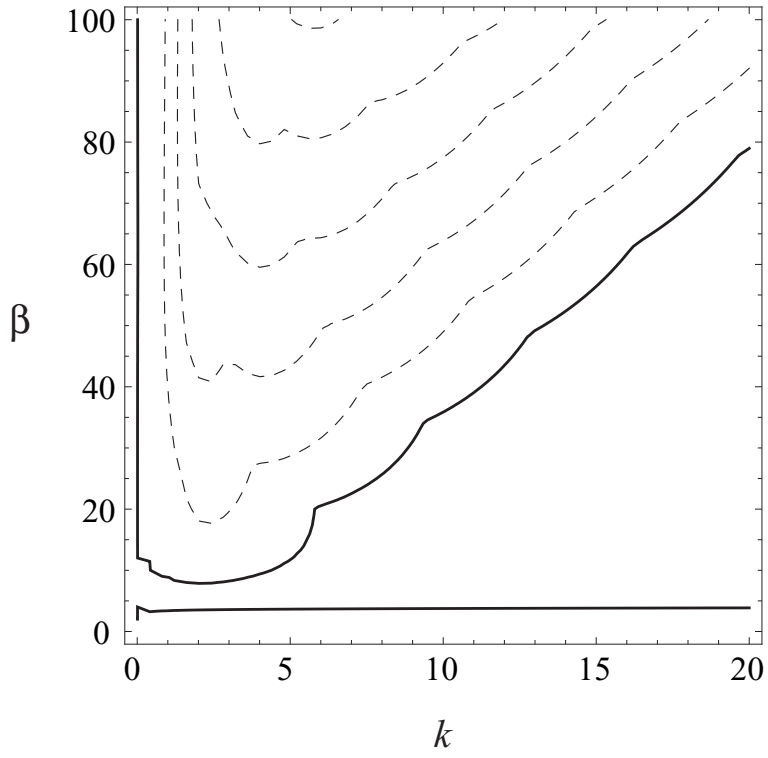

Figure 3.1: The contours of Im[ω] in the k-β plane for the case $\theta_n = 0.06$, $F = 0.5$, $C_f = 0.01$, $M = 1$ and $\gamma = 0.5$, where solid thick line indicates the neutral curve and the broken lines indicate the positive growth rates.

that $\mathbf{L}$ should be singular. Thus, we obtain

$$|\mathbf{L}| = 0 \tag{3.19}$$

The solution of the above equation takes the functional form

$$\omega = \omega(k, \beta; \theta_n, \theta_c, F, C_f, M, r, \gamma) \tag{3.20}$$

3.3 Results and discussions: Numerical solution

The contours of Im[ω] in the k-β plane for the case $\theta_n = 0.06$, $F = 0.5$, $C_f = 0.01$, $M = 1$ and $\gamma = 0.5$ are shown in Figure 3.1. The solid thick line indicates the neutral curve dividing the stable region and the unstable region. The broken lines are contours of positive growth rates. The figure shows that an unstable region appears in the range of large aspect ratios. It can be said that the critical (or minimum) aspect ratio inducing bed instability is approximately 8, below which the

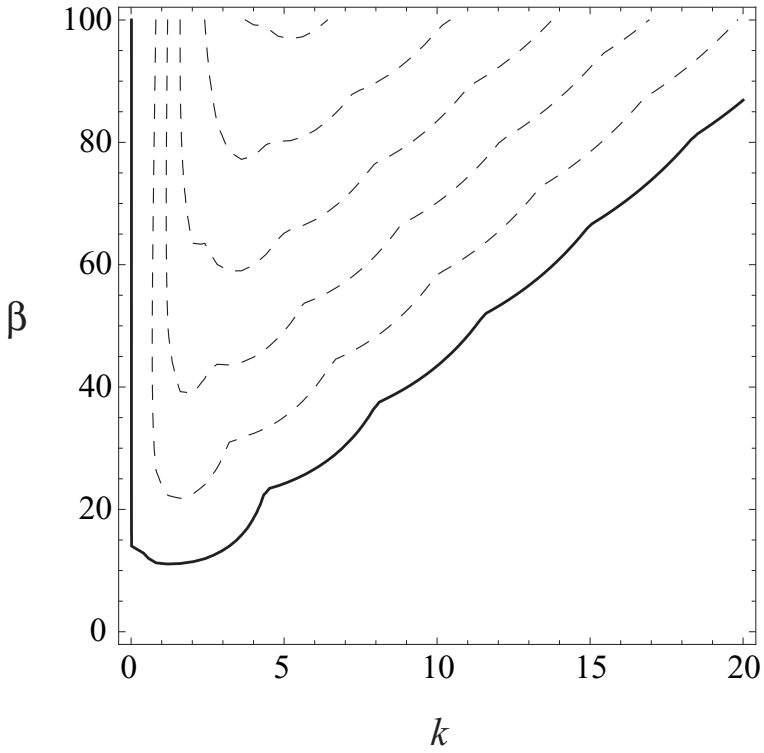

Figure 3.2: The contours of Im[ω] in the k-β plane for the case $\theta_n = 0.06$, $F = 0.5$, $C_f = 0.01$, $M = 1$ and $\gamma = 0$, where solid thick line indicates the neutral curve and the broken lines indicate the positive growth rates.

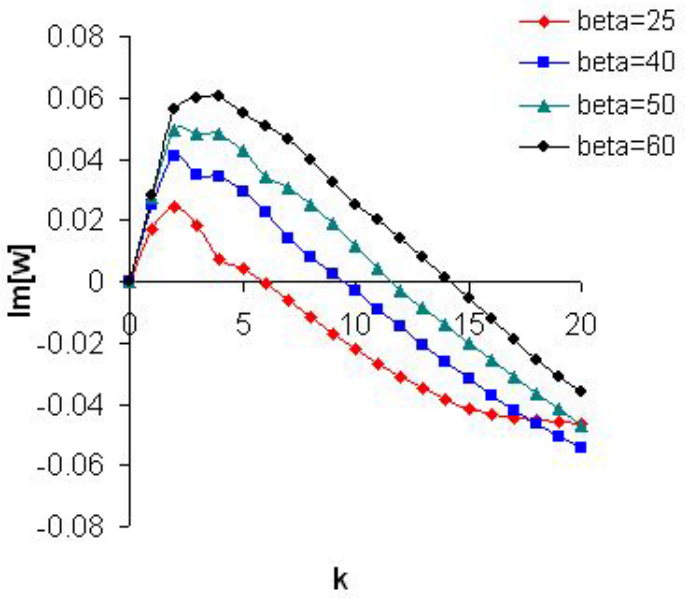

Figure 3.3: Plot of Im[ω] versus k, where, $\theta_n = 0.06$, $F = 0.5$, $C_f = 0.01$, $M = 1$ and $\gamma = 0.1$ for different aspect ratios β.

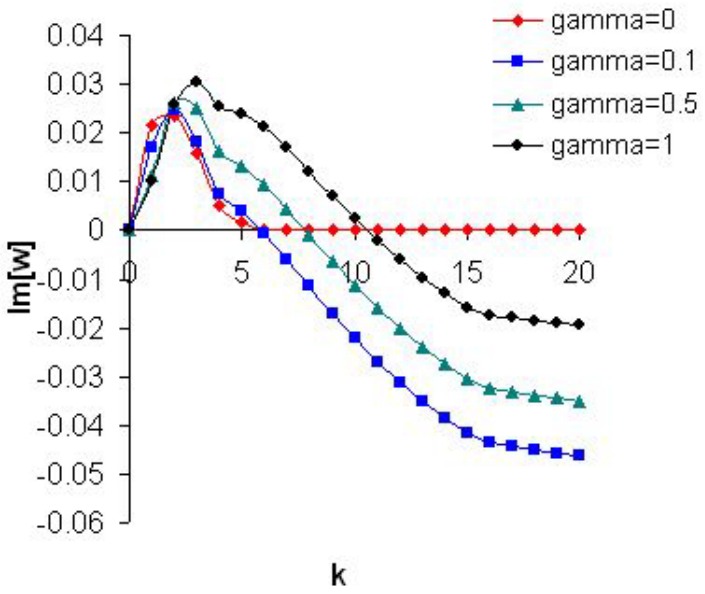

Figure 3.4: Plot of Im[ω] versus k, where, $\theta_n = 0.06$, $\beta = 25$, $C_f = 0.01$, $M = 1$, $F = 0.5$ for different bank erosion coefficient γ.

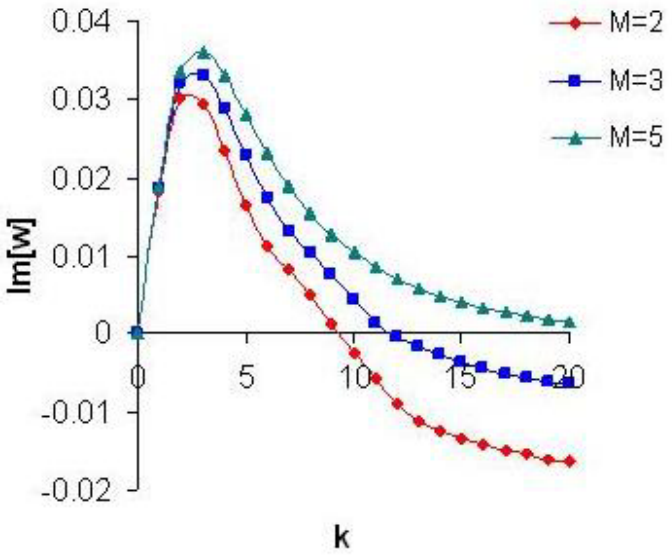

Figure 3.5: Plot of Im[ω] versus k, where, $\theta_n = 0.06$, $\beta = 25$, $C_f = 0.01$, $F = 0.5$, $\gamma = 0.1$ for different dimensionless bank height M.

flat bed is stable. There is an another unstable region in the range where β is smaller than approximately 3. Since the present shallow water formulation is not valid in the range of small β, the physical importance of this unstable region is not clear.

Figure 3.1 shows only the contours of the maximum Im[ω] corresponding to multiple bars with a variety of modes (lateral wavenumbers) as well as single alternate bars. The awkward shapes of contours in the figure are caused by the superposition of a number of contours of single alternate bars and multiple bars with different modes.

For comparison, the contours of Im[ω] in the k-β plane for the the case $\theta_n = 0.06$, $F = 0.5$, $C_f = 0.01$, $M = 1$ and $\gamma = 0$ are shown in Figure 3.2. Because γ represents the bank erodibility, the case $\gamma = 0$ corresponds to the case without bank erosion. It follows that Figure 3.2 shows the instability diagram of fluvial bars without bank erosion. It is found from Figures 3.1 and 3.2 that the unstable region expands slightly in the range of large k as γ increases. The bed becomes unstable in a wider range of wavenumbers if the bank is more erodible. There is a tendency of increasing bed instability due to bank erosion.

Figure 3.3 shows the plot of Im[ω] with the wavenumber k, where, $\theta_n = 0.06$, $F = 0.5$, $C_f = 0.01$, $M = 1$ and $\gamma = 0.1$ for different values of aspect ratios β. From this figure it can be seen that maximum growth rates increases with increasing the aspect ratios β. The curves are shifted from left to right with increasing wavenumber for different aspect ratios. The plot of Im[ω] with the wavenumber k, where, $\theta_n = 0.06$, $\beta = 25$, $C_f = 0.01$, $M = 1$ and $F = 0.5$ has been shown in the Figure 3.4 for different values of bank erosion coefficient γ. It is also seen from this figure that maximum growth rates increases with increasing values of bank erosion coefficient γ. Figure 3.5 shows the variation of Im[ω] with wave number k, where, $\theta_n = 0.06$, $\beta = 25$, $C_f = 0.01$, $F = 0.5$, $\gamma = 0.1$ for different dimensionless bank height M. From this figure it can be seen that the maximum growth rate increases with the increasing non-dimensional bank height.

Chapter 4

Analytical solution

We solve the differential system of equations involve in the linear stability analysis by analytically to see the effect of bank erosion coefficient γ on the bar instability and also compare the results of analytical solutions with the numerical solutions.

4.1 General solution at $O(A)$

We obtain general solution of the governing equations at $O(A)$ by the following way. The eqns. (3.3)–(3.6) form a differential system with respect to the four unknown variables U_1, V_1, H_1 and Z_1, which can be solved with the four boundary conditions (3.14)–(3.15) in the following manner. Linearly independent solutions are denoted by

$$(U_1, V_1, H_1, Z_1) = (u, v, h, z) \exp \alpha y \tag{4.1}$$

Substituting the above equations into (3.3)–(3.5), we obtain the algebraic equation in the matrix form

$$\mathsf{L}(\alpha) \cdot \boldsymbol{u} = \boldsymbol{r}(\alpha)\, z \tag{4.2}$$

where

$$\mathsf{L}(\alpha) = \begin{bmatrix} \mathrm{i}k + 2\beta C_f & 0 & \mathrm{i}kF^{-2} - \beta C_f \\ 0 & \mathrm{i}k + \beta C_f & \alpha F^{-2} \\ \mathrm{i}k & \alpha & \mathrm{i}k \end{bmatrix} \tag{4.3}$$

$$\boldsymbol{r}(\alpha) = \begin{bmatrix} -\mathrm{i}kF^{-2} \\ -\alpha F^{-2} \\ 0 \end{bmatrix}, \quad \boldsymbol{u} = \begin{bmatrix} u \\ v \\ h \end{bmatrix} \tag{4.4a, b}$$

The above equations can be easily solved to show that u, v and h are all expressed in the form of multiples of z, such that

$$u = f_u(\alpha)z, \quad v = f_v(\alpha)z, \quad h = f_h(\alpha)z \tag{4.5a, b, c}$$

where $f_u(\alpha)$, $f_v(\alpha)$ and $f_h(\alpha)$ are defined by

$$\begin{bmatrix} f_u(\alpha) \\ f_v(\alpha) \\ f_h(\alpha) \end{bmatrix} = \mathbf{L}^{-1}(\alpha) \cdot \boldsymbol{r}(\alpha) \tag{4.6}$$

Substituting (4.5) into (3.6), we obtain an algebraic equation in the following form:

$$\mathcal{A}\alpha^4 + \mathcal{B}\alpha^2 + \mathcal{C} = 0 \tag{4.7}$$

The four solutions of the above equation is obtained and among the four solutions, either of the following two solutions with positive signs before the radical sign

$$\sqrt{\frac{-\mathcal{B} + \sqrt{\mathcal{B}^2 - 4\mathcal{A}\mathcal{C}}}{2\mathcal{A}}}, \quad \sqrt{\frac{-\mathcal{B} - \sqrt{\mathcal{B}^2 - 4\mathcal{A}\mathcal{C}}}{2\mathcal{A}}} \tag{4.8a, b}$$

is denoted by α_a, and the other α_b. The four solutions are then written in the form

$$\alpha_1 = \alpha_a, \quad \alpha_2 = -\alpha_a, \quad \alpha_3 = \alpha_b, \quad \alpha_4 = -\alpha_b \tag{4.9}$$

Substituting α obtained in the above into (4.5), we obtain

$$u_i = f_u(\alpha_i)z_i, \quad v_i = f_v(\alpha_i)z_i, \quad h_i = f_h(\alpha_i)z_i, \quad (i = 1, 2, 3, 4) \tag{4.10}$$

General solutions are expressed as an exponential function. After some tedious calculation, with the use of cosh and sinh, the general solutions can be written in

the form

$$U_1 = \bar{z}_a f_u(\alpha_a)\cosh\alpha_a y + z_a f_u(\alpha_a)\sinh\alpha_a y + \bar{z}_b f_u(\alpha_b)\cosh\alpha_b y + z_b f_u(\alpha_b)\sinh\alpha_b y \tag{4.11a}$$

$$V_1 = z_a f_v(\alpha_a)\cosh\alpha_a y + \bar{z}_a f_v(\alpha_a)\sinh\alpha_a y + z_b f_v(\alpha_b)\cosh\alpha_b y + \bar{z}_b f_v(\alpha_b)\sinh\alpha_b y \tag{4.11b}$$

$$H_1 = \bar{z}_a f_h(\alpha_a)\cosh\alpha_a y + z_a f_h(\alpha_a)\sinh\alpha_a y + \bar{z}_b f_h(\alpha_b)\cosh\alpha_b y + \bar{z}_b f_h(\alpha_b)\sinh\alpha_b y \tag{4.11c}$$

$$Z_1 = \bar{z}_a\cosh\alpha_a y + z_a\sinh\alpha_a y + \bar{z}_b\cosh\alpha_b y + z_b\sinh\alpha_b y \tag{4.11d}$$

Note that, as found from (3.3)–(3.6), there is a phase difference of $\pi/2$ between V_1 and the other three variables U_1, H_1 and Z_1, and therefore, the coefficients of cosh and sinh of U_1, H_1 and Z_1, $\bar{z}_i$ and z_i, are corresponding to the coefficients of sinh and cosh of V_1, $\bar{z}_i$ and z_i, respectively.

4.2 γ expansion

In order to clarify the structure of solution, all the variables are expanded with the use of γ. That is

$$(U_1, V_1, H_1, Z_1) = (U_{10}, V_{10}, H_{10}, Z_{10}) + \gamma\,(U_{11}, V_{11}, H_{11}, Z_{11}) \tag{4.12}$$

Correspondingly, the complex angular frequency ω is also expanded as

$$\omega = \omega_0 + \gamma\omega_1 \tag{4.13}$$

where, γ is a small parameter such that $O(\gamma^2)$ terms vanish.

We substitute the above expansions into the governing equations, and obtain the solution up to $O(\gamma)$. Before proceeding further, we have to specify the phase shift between right and left banks. The phase shift can be arbitrary, but we consider two simple cases, herein, which are commonly observed in the field. One is the case of the both banks being in phase as shown in Figs. 2.1 and 2.3, and the other is the case of the both banks being out of phase as shown in Fig. 2.2.

4.2.1 The case of both banks being in phase

At first the solution has been done for the simplest cases, both banks being in phase. The following relation holds in that case

$$R_1 = L_1 \tag{4.14}$$

It is then found, from the boundary conditions that V_1 is an even function and symmetrical with respect to the x axis, while U_1 and Z_1 are odd functions and symmetrical with respect to the origin.

Substituting the (4.12)–(4.13) into (3.3)–(3.6), we obtain the following results at each order of γ. At $O(1)$ i.e. the lowest order of γ, we obtain the following equations

$$(\mathrm{i}k + 2\beta C_f)\, U_{10} + \left(\mathrm{i}kF^{-2} - \beta C_f\right) H_{10} + \mathrm{i}kF^{-2} Z_{10} = 0 \tag{4.15}$$

$$(\mathrm{i}k + \beta C_f)\, V_{10} + F^{-2}\frac{\mathrm{d}H_{10}}{\mathrm{d}y} + F^{-2}\frac{\mathrm{d}Z_{10}}{\mathrm{d}y} = 0 \tag{4.16}$$

$$\mathrm{i}kU_{10} + \frac{\mathrm{d}V_{10}}{\mathrm{d}y} + \mathrm{i}kH_{10} = 0 \tag{4.17}$$

$$-\mathrm{i}\omega_0 Z_{10} + 24\mathrm{i}k\theta_n \left(\theta_n - \theta_c\right)^{1/2} U_{10} + 8\left(\theta_n - \theta_c\right)^{3/2} \frac{\mathrm{d}V_{10}}{\mathrm{d}y} - \frac{8\left(\theta_n - \theta_c\right)^{3/2} r}{\beta\theta_n^{1/2}} \frac{\mathrm{d}^2 Z_{10}}{\mathrm{d}y^2} = 0 \tag{4.18}$$

At $O(1)$ i.e. the lowest order of γ, from the boundary condition, we obtain

$$V_{10}\left(\frac{1}{2}\right) = 0, \quad \frac{\mathrm{d}Z_{10}\left(\frac{1}{2}\right)}{\mathrm{d}y} = 0 \tag{4.19a, b}$$

From the symmetry of solutions, four boundary conditions are reduced to be above two. The solutions of the above differential system take the form

$$U_{10} = z_{10,a} f_u(\alpha_a) \sinh \alpha_a y + z_{10,b} f_u(\alpha_b) \sinh \alpha_b y \tag{4.20a}$$

$$V_{10} = z_{10,a} f_v(\alpha_a) \cosh \alpha_a y + z_{10,b} f_v(\alpha_b) \cosh \alpha_b y \tag{4.20b}$$

$$H_{10} = z_{10,a} f_h(\alpha_a) \sinh \alpha_a y + z_{10,b} f_h(\alpha_b) \sinh \alpha_b y \tag{4.20c}$$

$$Z_{10} = z_{10,a} \sinh \alpha_a y + z_{10,b} \sinh \alpha_b y \tag{4.20d}$$

where the above solutions satisfy the boundary conditions (4.19) only when $\alpha_a = n\pi\mathrm{i}$ $(n = 1, 3, 5, \cdots)$ and $z_{10,b} = 0$, or $\alpha_b = n\pi\mathrm{i}$ and $z_{10,a} = 0$. We assume

$$\alpha_a = n\pi\mathrm{i} \quad (n = 1, 3, 5, \cdots) \quad \text{and} \quad z_{10,b} = 0 \tag{4.21a, b}$$

Note that, when α_a can be written in the above equation, α_b can be expressed by

$$\alpha_b = \sqrt{n^2\pi^2 - \frac{\mathcal{B}}{\mathcal{A}}} \tag{4.22}$$

Substituting the above equations into (4.18), we obtain following equation

$$\omega_0 = 24k\theta_n(\theta_n - \theta_c)^{1/2} f_u(\alpha_a) - \mathrm{i}8(\theta_n - \theta_c)^{3/2}\alpha_a f_v(\alpha_a) + \mathrm{i}\frac{8(\theta_n - \theta_c)^{3/2} r}{\beta\theta_n^{1/2}}\alpha_a^2 \tag{4.23}$$

The equation (4.23) is the solution of the original bar instability problem.

At $O(\gamma)$, we obtain the following equations

$$(\mathrm{i}k + 2\beta C_f)\, U_{11} + \left(\mathrm{i}kF^{-2} - \beta C_f\right) H_{11} + \mathrm{i}kF^{-2} Z_{11} = 0 \tag{4.24}$$

$$(\mathrm{i}k + \beta C_f)\, V_{11} + F^{-2}\frac{\mathrm{d}H_{11}}{\mathrm{d}y} + F^{-2}\frac{\mathrm{d}Z_{11}}{\mathrm{d}y} = 0 \tag{4.25}$$

$$\mathrm{i}kU_{11} + \frac{\mathrm{d}V_{11}}{\mathrm{d}y} + \mathrm{i}kH_{11} = 0 \tag{4.26}$$

$$-\mathrm{i}\omega_0 Z_{11} + 24\mathrm{i}k\theta_n\left(\theta_n - \theta_c\right)^{1/2} U_{11} + 8\left(\theta_n - \theta_c\right)^{3/2}\frac{\mathrm{d}V_{11}}{\mathrm{d}y} - \frac{8\left(\theta_n - \theta_c\right)^{3/2} r}{\beta\theta_n^{1/2}}\frac{\mathrm{d}^2 Z_{11}}{\mathrm{d}y^2} = \mathrm{i}\omega_1 Z_{10} \tag{4.27}$$

At $O(\gamma)$, from the boundary condition, we obtain

$$\frac{\omega_0}{k} MV_{11}\left(\frac{1}{2}\right) + \frac{\omega_1}{k} MV_{10}\left(\frac{1}{2}\right) = -\frac{8\left(\theta_n - \theta_c\right)^{3/2} r}{\beta\theta_n^{1/2}}\frac{\mathrm{d}Z_{11}\left(\frac{1}{2}\right)}{\mathrm{d}y} \tag{4.28}$$

$$\frac{\omega_0}{k} MV_{11}\left(\frac{1}{2}\right) + \frac{\omega_1}{k} MV_{10}\left(\frac{1}{2}\right) = -2\theta_n U_{10}\left(\frac{1}{2}\right) \tag{4.29}$$

It is found that (4.27) has the same form as (4.18) except for the right hand side. The homogeneous part of U_{11}, V_{11}, H_{11} and Z_{11} in (4.27) has the same form as that of U_{10}, V_{10}, H_{10} and Z_{10} in (4.18), and only the inhomogeneous part is different. In addition, the inhomogeneous part has the same form as the solution of homogeneous

equation. The solution of the inhomogeneous differential system can be expressed by the combination of the general solution and the special solution in the form

$$U_{11} = u_{11,a}\sinh\alpha_a y + u_{11,b}\sinh\alpha_b y + u_{11,s} y\cosh\alpha_a y \tag{4.30a}$$

$$V_{11} = v_{11,a}\cosh\alpha_a y + v_{11,b}\cosh\alpha_b y + v_{11,s} y\sinh\alpha_a y \tag{4.30b}$$

$$H_{11} = h_{11,a}\sinh\alpha_a y + h_{11,b}\sinh\alpha_b y + h_{11,s} y\cosh\alpha_a y \tag{4.30c}$$

$$Z_{11} = z_{11,a}\sinh\alpha_a y + z_{11,b}\sinh\alpha_b y + z_{11,s} y\cosh\alpha_a y \tag{4.30d}$$

Substituting the above equations into (4.24)–(4.26), we obtain

$$\begin{aligned}
&\left[(\mathrm{i}k + 2\beta C_f)\, u_{11,a} + \left(\mathrm{i}kF^{-2} - \beta C_f\right) h_{11,a} + \mathrm{i}kF^{-2} z_{11,a}\right]\sinh\alpha_a y \\
&\quad + \left[(\mathrm{i}k + 2\beta C_f)\, u_{11,b} + \left(\mathrm{i}kF^{-2} - \beta C_f\right) h_{11,b} + \mathrm{i}kF^{-2} z_{11,b}\right]\sinh\alpha_b y \\
&+ \left[(\mathrm{i}k + 2\beta C_f)\, u_{11,s} + \left(\mathrm{i}kF^{-2} - \beta C_f\right) h_{11,s} + \mathrm{i}kF^{-2} z_{11,s}\right] \quad y\cosh\alpha_a y = 0
\end{aligned} \tag{4.31}$$

$$\begin{aligned}
&\left[(\mathrm{i}k + \beta C_f)\, v_{11,a} + \mathrm{i}\alpha_a F^{-2} h_{11,a} + \mathrm{i}\alpha_a F^{-2} z_{11,a} + F^{-2} h_{11,s} + F^{-2} z_{11,s}\right]\cosh\alpha_a y \\
&\quad + \left[(\mathrm{i}k + \beta C_f)\, v_{11,b} + \mathrm{i}\alpha_b F^{-2} h_{11,b} + \mathrm{i}\alpha_b F^{-2} z_{11,b}\right]\cosh\alpha_b y \\
&- \left[(\mathrm{i}k + \beta C_f)\, v_{11,s} + \mathrm{i}\alpha_a F^{-2} h_{11,s} + \mathrm{i}\alpha_a F^{-2} z_{11,s}\right] \quad y\sinh\alpha_a y = 0
\end{aligned} \tag{4.32}$$

$$\begin{aligned}
&[\mathrm{i}k u_{11,a} + \mathrm{i}\alpha_a v_{11,a} + \mathrm{i}k h_{11,a} + v_{11,s}]\sinh\alpha_a y \\
&\quad + [\mathrm{i}k u_{11,b} + \mathrm{i}\alpha_b v_{11,b} + \mathrm{i}k h_{11,b}]\sinh\alpha_b y \\
&\quad + [\mathrm{i}k u_{11,s} + \mathrm{i}\alpha_a v_{11,s} + \mathrm{i}k h_{11,s}] \quad y\cosh\alpha_a y = 0
\end{aligned} \tag{4.33}$$

Because $\sinh\alpha_a y$, $\sinh\alpha_b y$, $y\cosh\alpha_a y$, $\cosh\alpha_a y$, $\cosh\alpha_b y$, and $y\sinh\alpha_a y$ are linearly independent in the above equations, each coefficient should vanish. Therefore, we obtain

$$\mathbf{L}(\alpha_a)\cdot\begin{bmatrix} u_{11,a} \\ v_{11,a} \\ h_{11,a} \end{bmatrix} = \boldsymbol{r}(\alpha_a) z_{11,a} + \begin{bmatrix} 0 \\ -F^{-2}\left(h_{11,s} + z_{11,s}\right) \\ -v_{11,s} \end{bmatrix} \tag{4.34}$$

$$\mathbf{L}(\alpha_b)\cdot\begin{bmatrix} u_{11,b} \\ v_{11,b} \\ h_{11,b} \end{bmatrix} = \boldsymbol{r}(\alpha_b) z_{11,b}, \quad \mathbf{L}(\alpha_a)\begin{bmatrix} u_{11,s} \\ v_{11,s} \\ h_{11,s} \end{bmatrix} = \boldsymbol{r}(\alpha_a) z_{11,s} \tag{4.35a, b}$$

Solving (4.35) by using (4.6), we obtain

$$\begin{bmatrix} u_{11,b} \\ v_{11,b} \\ h_{11,b} \end{bmatrix} = \begin{bmatrix} f_u(\alpha_b) \\ f_v(\alpha_b) \\ f_h(\alpha_b) \end{bmatrix} z_{11,b}, \quad \begin{bmatrix} u_{11,s} \\ v_{11,s} \\ h_{11,s} \end{bmatrix} = \begin{bmatrix} f_u(\alpha_a) \\ f_v(\alpha_a) \\ f_h(\alpha_a) \end{bmatrix} z_{11,s} \tag{4.36a, b}$$

Solving (4.34) by using (4.36), we obtain

$$\begin{bmatrix} u_{11,a} \\ v_{11,a} \\ h_{11,a} \end{bmatrix} = \begin{bmatrix} f_u(\alpha_a) \\ f_v(\alpha_a) \\ f_h(\alpha_a) \end{bmatrix} z_{11,a} + \begin{bmatrix} g_u(\alpha_a) \\ g_v(\alpha_a) \\ g_h(\alpha_a) \end{bmatrix} z_{11,s} \tag{4.37}$$

where

$$\begin{bmatrix} g_u(\alpha) \\ g_v(\alpha) \\ g_h(\alpha) \end{bmatrix} = \mathbf{L}(\alpha)^{-1} \begin{bmatrix} 0 \\ -F^{-2}\left[f_h(\alpha)+1\right] \\ -f_v(\alpha) \end{bmatrix} \tag{4.38}$$

Substituting the above equations into the Exner equation (4.27) and eliminating some terms according to the result of (4.23) at $O(1)$, we obtain the following equation

$$\begin{aligned} 24\mathrm{i}k\theta_n\left(\theta_n-\theta_c\right)^{1/2} g_u(\alpha_a) z_{11,s} + 8\left(\theta_n-\theta_c\right)^{3/2}\left[\alpha_a g_v(\alpha_a) + f_v(\alpha_a)\right] z_{11,s} \\ -\frac{8\left(\theta_n-\theta_c\right)^{3/2} r}{\beta\theta_n^{1/2}} 2\alpha_a z_{11,s} - \mathrm{i}\omega_1 z_{10} = 0 \end{aligned} \tag{4.39}$$

If the relation between $z_{11,s}$ and z_{10} can be found, we can obtain ω_1 from the above equation. The relation between $z_{11,s}$ and z_{10} is obtained from the boundary conditions (4.28) and (4.29) as follows.

From the results at $O(1)$, we obtain $U_{10}(1/2)$ and $V_{10}(1/2)$ in the form

$$U_{10}\left(\frac{1}{2}\right) = u_{10}\mathrm{i}\sin\frac{n\pi}{2} = \begin{cases} \mathrm{i}u_{10} & \text{when} \quad n = \text{odd} \\ 0 & \text{when} \quad n = \text{even} \end{cases} \tag{4.40}$$

$$V_{10}\left(\frac{1}{2}\right) = 0 \tag{4.41}$$

In addition at $O(\gamma)$, $V_{11}(1/2)$ and $\mathrm{d}Z_{11}(1/2)/\mathrm{d}y$ can be obtained in the form

$$\begin{aligned} V_{11}\left(\frac{1}{2}\right) &= z_{11,b} f_v(\alpha_b) \cosh\frac{\alpha_b}{2} + z_{11,s}\frac{f_v(\alpha_a)}{2}\mathrm{i}\sin\frac{n\pi}{2} \\ &= \begin{cases} z_{11,b} f_v(\alpha_b) \cosh\dfrac{\alpha_b}{2} + z_{11,s}\mathrm{i}\dfrac{f_v(\alpha_a)}{2} & \text{when} \quad n = \text{odd} \\ 0 & \text{when} \quad n = \text{even} \end{cases} \end{aligned} \tag{4.42}$$

$$\begin{aligned} \frac{\mathrm{d}Z_{11}\left(\frac{1}{2}\right)}{\mathrm{d}y} &= z_{11,b}\alpha_b \cosh\frac{\alpha_b}{2} - z_{11,s}\frac{n\pi}{2}\sin\frac{n\pi}{2} \\ &= \begin{cases} z_{11,b}\alpha_b \cosh\dfrac{\alpha_b}{2} - z_{11,s}\dfrac{n\pi}{2} & \text{when} \quad n = \text{odd} \\ 0 & \text{when} \quad n = \text{even} \end{cases} \end{aligned} \tag{4.43}$$

Substituting (4.40)–(4.43) into (4.28)–(4.29), we obtain the value of $z_{11,s}$ as a function of z_{10}. Substituting the value of $z_{11,s}$ into (4.39), we obtain ω_1. In this case, we evaluate the values of ω from equation (4.13) by using the values of ω_0 and ω_1.

4.2.2 The case of both banks being out of phase

The solution has been done for the another case of both banks being completely out of phase (Fig. 2.2). Such that

$$R_1 = -L_1 \tag{4.44}$$

In this case, from the boundary conditions we find that V_1 is an odd function and symmetrical with respect to the origin, while U_1 and Z_1 are even functions and symmetrical with respect to the x axis. In this case, similar calculation has been done (except sin and cos are replaced by cos and sin respectively) as for the case both bank being in phase. The values of lateral wavenumbers n is even in this case. For evaluating ω_1 in this case the relation between $z_{11,s}$ and z_{10} is obtained from (4.28) and (4.29) by following ways.

From the results at $O(1)$, we obtain $U_{10}(1/2)$ and $V_{10}(1/2)$ in the form

$$U_{10}\left(\frac{1}{2}\right) = u_{10}\mathrm{i}\cos\frac{n\pi}{2} = \begin{cases} 0 & \text{when} \quad n = \text{odd} \\ -\mathrm{i}u_{10} & \text{when} \quad n = \text{even} \end{cases} \tag{4.45}$$

$$V_{10}\left(\frac{1}{2}\right) = 0 \tag{4.46}$$

In addition at $O(\gamma)$, $V_{11}(1/2)$ and $\mathrm{d}Z_{11}(1/2)/\mathrm{d}y$ can be obtained in the form

$$\begin{aligned} V_{11}\left(\frac{1}{2}\right) &= z_{11,b} f_v(\alpha_b) \sinh\frac{\alpha_b}{2} + z_{11,s}\frac{f_v(\alpha_a)}{2}\mathrm{i}\cos\frac{n\pi}{2} \\ &= \begin{cases} 0 & \text{when} \quad n = \text{odd} \\ z_{11,b} f_v(\alpha_b)\sinh\dfrac{\alpha_b}{2} - z_{11,s}\mathrm{i}\dfrac{f_v(\alpha_a)}{2} & \text{when} \quad n = \text{even} \end{cases} \end{aligned} \tag{4.47}$$

$$\begin{aligned} \frac{\mathrm{d}Z_{11}\left(\frac{1}{2}\right)}{\mathrm{d}y} &= z_{11,b}\alpha_b \sinh\frac{\alpha_b}{2} - z_{11,s}\frac{n\pi}{2}\cos\frac{n\pi}{2} \\ &= \begin{cases} 0 & \text{when} \quad n = \text{odd} \\ z_{11,b}\alpha_b\cosh\dfrac{\alpha_b}{2} - z_{11,s}\dfrac{n\pi}{2} & \text{when} \quad n = \text{even} \end{cases} \end{aligned} \tag{4.48}$$

Substituting (4.45)–(4.48) into (4.28)–(4.29), we obtain the value of $z_{11,s}$ as a function of z_{10}. Substituting the value of $z_{11,s}$ into (4.34), we obtain ω_1. In this case, by using the values of ω_0 and ω_1, we obtain the values of ω from equation (4.13)

Chapter 5

Results and discussions: Analytical solution

5.1 Evaluation of bank erosion coefficient γ

In our study we consider γ is a coefficient of bank erosion which is assumed to be a function of the non-dimensional bed shear stress. We have evaluated our γ from field data based on the Hasegawa's bank erosion coefficient E_0 and also from the experimental data of Watanabe (2015). The bank erosion coefficient E_0 which depends on hydraulic factors as well as geotechnical properties of the bank has been discussed by Hasegawa (1989). He determined the values of bank erosion coefficient E_0 for three rivers in Hokkaido (Ishikari, Uryu and Mukawa river) and found that the values ranges between 0.92×10^{-7} to 19.17×10^{-7}.

According to Hasegawa (1989) (equation (14), pp.750), the rate of bank erosion is expressed by

$$\tilde{\zeta} = E_0 u_B \tag{5.1}$$

where, $\tilde{\zeta}$ is the bank erosion rate (channel migration rate), E_0 is the Hasegawa's bank erosion coefficient and u_B is the excess of near-bank depth-averaged stream-wise flow velocity over the mean value for the cross section.

In our study from (2.21) and (2.22) the bank erosion rate can be expressed as the following dimensional form

$$\tilde{\zeta} = \frac{\tilde{\gamma}(\theta - \theta_n)}{\tilde{M}} \tag{5.2}$$

where $\tilde{\gamma}$ is the dimensional version of the bank erosion coefficient while the γ itself is non-dimensional, defined by

$$\tilde{\gamma} = \frac{\gamma\sqrt{R_s g \tilde{d}_s^3}}{(1-\lambda_p)} \tag{5.3}$$

By using (2.30) and (3.1) in (5.2) and neglecting higher order terms, we obtained

$$\tilde{\zeta} = \frac{2\tilde{\gamma}\theta_n}{\tilde{M}}(AU_1) \tag{5.4}$$

By rewriting (5.4), we get

$$\tilde{\zeta} = \frac{2\gamma\theta_n\sqrt{R_s g \tilde{d}_s^3}}{(1-\lambda_p)\tilde{H}_n\tilde{U}_n}u_B \tag{5.5}$$

where $AU_1 = u_B/\tilde{U}_n$ and $\tilde{M} = \tilde{H}_n$ is assumed

By comparing (5.1) and (5.5), we obtained

$$\gamma = E_0\left(\frac{(1-\lambda_p)\tilde{H}_n\tilde{U}_n}{2\theta_n\sqrt{R_s g \tilde{d}_s^3}}\right) \tag{5.6}$$

We have evaluated γ from the above equation by using the values of the parameters on the right hand side. The bank erosion coefficient E_0 in equation (5.1) is obtained by means of calibration against field data. Parker (1982), Beck (1984) and Johannesson and Parker (1985) applied the formulation to various river reaches, and found E_0 to be in the range 10^{-8} to 10^{-7}, which is close to the Hasegawa's E_0. By using the average values of E_0, we calculated our γ by equation (5.6) for 116 sets of data obtained from different rivers in Japan. We found that γ ranges between 4.27×10^{-5} to 4.39×10^{-2} (Appendix B). From Watanabe's experiment (2015) we have taken the maximum bank erosion rate $\tilde{\zeta} = 0.65$ cm/min, $\tilde{U_n} = 0.276$ m/s, $\tilde{H_n} = 0.007$ m, $\theta_n = 0.056$, $\tilde{d_s} = 0.765$ mm and $u_B = 0.042$ m/s (assumed) to evaluate γ from (5.1) and (5.6), and found the value is 0.5.

5.2 Instability diagram of bars with bank erosion

The contours of $\mathrm{Im}[\omega_0 + \gamma\omega_1]$ in the k-β plane for the case $\theta_n = 0.06$, $F = 0.2$, $C_f = 0.01$, $M = 1$, $\gamma = 0$ (dashed line), $\gamma = 0.04$ (red dashed dotted line) and

$\gamma = 0.1$ (solid thick line) for different lateral wavenumbers n are shown in Fig. 5.1(a) in the case of both banks being in phase and (b) in the case of both banks being out of phase. We adopted 0.2 and 0.06 for F and θ_n, respectively, as typical values for gravel bed rivers in the field. However, other choices of those parameters result in qualitatively similar diagrams. All the curves shown in these figures are neutral instability curves. In Figure 5.1(a), the case $n = 1$ corresponds to single alternate bars, and the cases $n>1$ to multiple bars. Meanwhile, in Figure 5.1(b), the case $n = 2$ corresponds to double row bars, and the cases $n>2$ to multiple bars. In addition, n of odd numbers correspond to the case of both banks being in phase, and n of even numbers correspond to the case of both banks being out of phase.

In the all cases of lateral wavenumbers, the unstable regions generally expands in the direction of increasing k due to bank erosion. That tendency is remarkable especially in the case of single alternate bars ($n = 1$ in Fig. 5.1(a)). The expansion of unstable region in the direction of increasing k means that the wavelength of bars decreases. The implication is that excessive sediment supplied due to bank erosion causes the increase of bed instability, and the resulting decrease in the bar wavelength. We can also see from this figure that if the value of γ is smaller than 0.04, the effect of bank erosion is negligible at least in the instability diagram.

Discontinuous changes of neutral curves can be seen in the ranges of large aspect ratios and large wavenumbers in Fig. 5.1. In order to see the effect which parameter create this types of discontinuities, we have added the Figure 5.2 which shows the contours of $\mathrm{Im}[\omega_0 + \gamma\omega_1]$ in the k-β plane for the case $\theta_n = 0.06$, $C_f = 0.01$, $M = 1$ and $\gamma = 0.1$ for different values of Froude number F. All the curve shown in this figure is neutral instability curves. It is found from this Figure that the discontinuity is not observed in the case of large Froude numbers. From these results, it is suspected that the term at $O(\gamma)$ becomes too large for the γ expansion to be valid. The analysis proposed herein is assumed to be applicable only in the ranges of relatively small aspect ratios and wavenumbers, and large Froude numbers.

The contours of $\mathrm{Im}[\omega_1]$ in the k-β plane for $n = 1$ (single alternate bars), $n = 2$ (double row bars) and $n = 3$ (multiple bars) are shown in Figs. 5.3 (a), (b) and (c) respectively, where $\theta_n = 0.06$, $F = 0.2$, $C_f = 0.01$, $M = 1$ and ω_1 is the growth rate of perturbation in the order of γ. The solid thick line shows the neutral curve which

divides the positive and negative regions of ω_1. The dotted lines and dashed-dotted lines show the positive and negative contours of ω_1 respectively. In these figures it is visible that ω_1 have a tendency to stabilize the flat bed in the range of small wavenumbers, and in the range of large wavenumbers and large aspect ratios. That tendency is slightly higher for multiple bars than single alternate and double row bars. Figure 5.3 (a) and (b), also shows that the flat bed is destabilized in the region where β is smaller than approximately 2. Since the present shallow water formulation is not valid in the range of small β, the physical meaning of this unstable region is not clear.

It can be observed from Figure 5.3 (c), that for multiple bars destabilization region is also expanded higher than single alternate and double row bars in the ranges of relatively small aspect ratios. Another destabilization region has been seen in the range of large aspect ratios and large wavenumbers from this figure.

The contours of $\mathrm{Im}[\omega_0 + \gamma\omega_1]$ in the k-β plane for the case $\theta_n = 0.06$, $F = 0.2$, $C_f = 0.01$, $\gamma = 0.1$, $M = 1$ (solid thick line) and $M = 1.1$ (red thick line) for different lateral wavenumbers n are shown in Fig.5.4 (a) in the case of both banks being in phase and (b) in the case of both banks being out of phase . All the curve shown in this figure is neutral instability curves. In this figure the case $n = 1$ corresponds to single alternate bars, the case $n = 2$ corresponds to double row bars, and the cases $n>2$ to multiple bars. It can be seen from this figure that, the unstable regions generally expands in the direction of increasing wavenumbers due to increasing the dimensionless bank height M for all cases of lateral wavenumbers. That tendency is remarkable especially in the case of single alternate bars. The expansion of unstable region in the direction of increasing wavenumber k means that the wavelength of bars decreases.

5.3 Validity limit of the γ expansion

In order to see the validity limit of γ, we have compared the analytical solution with the numerical solution for different values of γ. We neglected the higher order terms of γ and consider only the first order terms. The contours of $\mathrm{Im}[\omega]$ in the k-β plane for the case $\theta_n = 0.06$, $F = 0.5$, $C_f = 0.01$, $M = 1$, for different values of $\gamma = 0$, 0.1,

0.6 and 0.7 has been shown in the Figs. 5.5 (a), (b), (c) and (d) respectively. The analytical solution is shown by the broken lines, and the numerical solution by the solid line. In the Figure 5.5 (a), we can see that the analytical solution shows the good agreement with numerical solution when there is no bank erosion (i.e. $\gamma = 0$).

In the case of the numerical solution, only the maximum growth rate can be calculated, and therefore, the neutral curve corresponds to all the wavenumbers (solid line). In the case of analytical solution, however, neutral curves corresponding to different wavenumbers can be separately obtained (broken lines).

We can seen in the Figures 5.5 (b) and (c) that up to $\gamma = 0.6$, the envelope of all the neutral curves of analytical solution agrees well with the neutral curve of numerical solution in the range of large wavenumbers. It is found, however, the agreement is not good in the range of small wave numbers.

From the Fig. 5.5 (c), we can see that the separation started between analytical solution and numerical solution for $\gamma = 0.7$ with alone increasing the wavenumber. So it can be said that if we further increases the value of γ, the higher deviation will be created between numerical solution and analytical solution, alone with increasing the wavenumber. We can also see that with increasing the value of γ, the deviation become slightly larger in the ranges of small wavenumbers. It can be said that ω_1 may have an effect for that deviation in the ranges of small wavenumbers.

5.4 Comparison of the bed topography with Watanabe's experiments

An experiment has been conducted (2015) by Watanabe in the River Disaster Prevention Laboratory of Kitami Istitute of Technology by varying the width of the water way of the channel for five cases (Case1, Case2, Case3, Case4 and Case5). From his analysis he found an relationship of the moving speed of the sandbar and the erosion rate of the river bank. If sanbar movement speed is faster impact on the river bank erosion is less and for movement speed is slow, impact on the river-bank erosion is higher. He also found that single row sandbar (Case1 and Case2) which dominate sandbar development, and double row sandbar (Case3 and Case4) dominant plane instability.

Bed elevation is not important in the linear stability analysis as amplitude A is assumed to be infinitesimally small. We have compared only the qualitative similarities between the bed level of present study and the bed level of Watanabe's experiments. Figure 5.6 shows the comparison of bed level between (a) present study when the both of the bank being in phase and (b) Watanabe's experiment for case1 (when channel width 0.25m). Continuous development of alternate bars have been visible from Figure 5.6 (a), so that each bend contains one alternate bar. Figure 5.6 (b) shows that river channel is widened almost simultaneously sandbar (single alternate bars) is being formed. The riverbank is eroded and the flow path is curved which finally formed meandering channel.

Figure 5.7 shows the comparison of bed level between (a) present study when the both of the bank being out of phase and (b) Watanabe's experiment for case3 (when channel width 0.45m). Double row bars formation have been found on Figure 5.7 (a). From Figure 5.7 (b) we can observed that river channel is widened and double row bars have been formed. Riverbank erosion occurs but meandering channel is not formed, finally the shape of the channel become snake-like ball.

5.5 Comparison with data

We assume that the wavelength of the maximum instability is the rough estimate of the wavelength of the finite amplitude bars realized in nature. The predicted wavelengths λ_c corresponding to maximum growth rates $\mathrm{Im}[\omega_0 + \gamma\omega_1]$ have been calculated from our analysis. We have plotted the predicted wavelengths λ_c from our analysis with the observed wavelengths λ from field data in the Figure 5.8 to compare the wavelength of bars predicted by our analysis with field data.

Ikeda *et al.* (1981) performed linear stability analysis of a sinuous channel with erodible banks by using the bank erosion equation and bend equation. He found conditions for the lateral bend amplitude to grow or die on the basis of the wavenumber of neutral instability and the critical wavenumber. According to Ikeda *et al.* (1981) (equation (24a), pp.370), the wavenumber k_{max} at which instability is maximized are obtained

$$k_{max} = 1.50C_f \tag{5.7}$$

The prediction wavelengths λ_c corresponding wavenumbers k_{max} are obtained

$$\lambda_c = \frac{2\pi H_0}{1.50 C_f} \tag{5.8}$$

where H_0 is the flow depth in normal condition.

We have calculated the prediction wavelength λ_c from meandering analysis performed by Ikeda *et al.* (1981) by using equation (5.8). We have plotted the predicted wavelengths λ_c from analysis of meandering with the observed wavelengths λ from field data in the Figure 5.9 to compare the wavelength of bars predicted by meandering analysis with field data. The values of λ_c calculated from field data has been shown in Appendix B.

From the Figures 5.8 and 5.9, we can see that both relations provide rough agreement. The data scatter less about the prediction of our present study of bar instability than meandering analysis. It can be said that the prediction obtained in our analysis agree better with the field data than that obtained in the analysis of meandering performed by Ikeda et al. (1981). This implies that the some cases of meandering can possibly be explained by our theory of the bar instability with bank erosion.

We also test our analysis with the use of experimental data obtained by Watanabe, Corasato and Hasegawa as shown in Figure 5.10. The plots are in terms of predicted wavelengths λ_c and observed wavelengths λ rather than wave number. The relation shows a reasonable agreement between the prediction and the experimental data. The major hydraulic parameters from the experiments of Watanabe (Case 1-5), and Corasato, and Hasegawa has been shown in Table 5.1 .

Table 5.1: Hydraulic parameters from the experiments of Watanabe (Case 1-5), and Corasato, and Hasegawa.

Expt. No.	S	d_s	F	θ_n	θ_c	λ_c	λ
Case 1	0.01	0.765	1.047	0.056	0.034	1.06	2.07
Case 2	0.01	0.765	1.055	0.056	0.034	1.19	1.00
Case 3	0.01	0.765	1.055	0.056	0.034	1.69	2.33
Case 4	0.01	0.765	1.055	0.056	0.034	2.23	3.20
Case 5	0.01	0.765	1.055	0.056	0.034	2.80	1.38
Crosato Expt.	0.004	0.238	0.339	0.467	0.06	2.03	3.00
Hasegawa Expt.	0.02	0.455	2.617	0.052	0.04	1.93	1.48

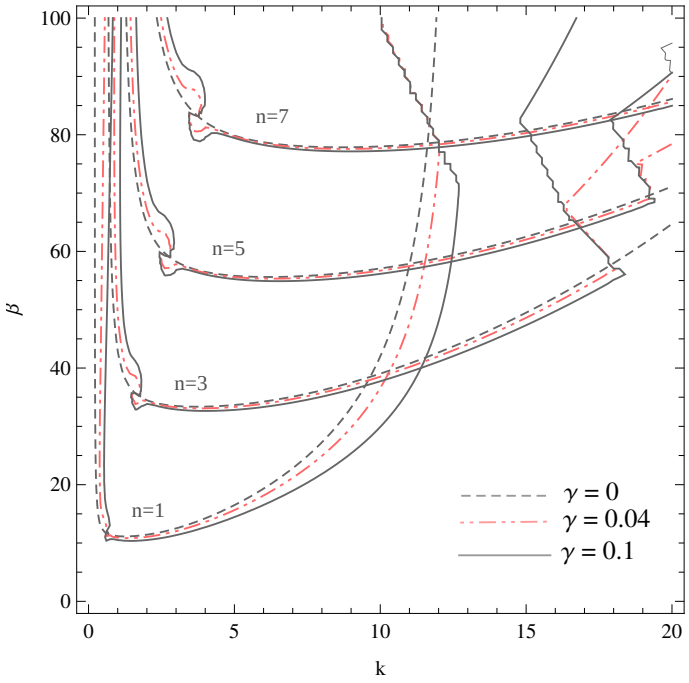

(a) Case of both banks being in phase

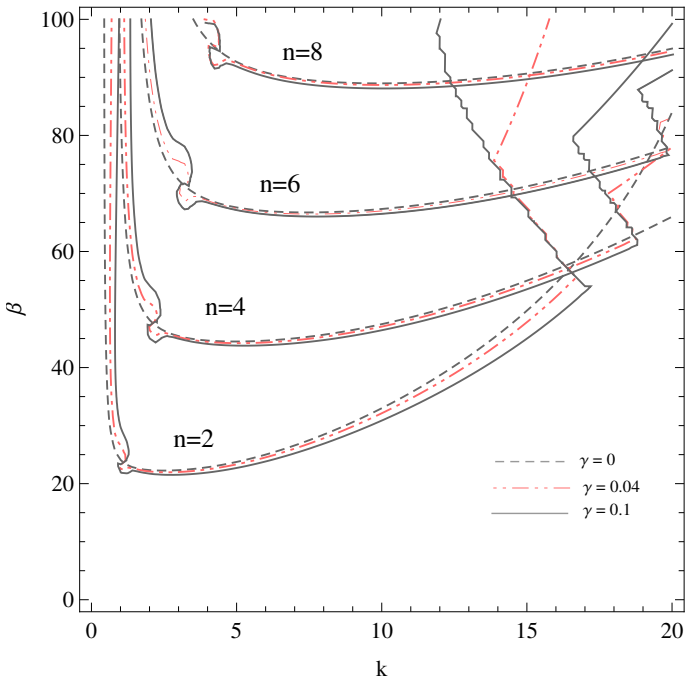

(b) Case of both banks being out of phase

Figure 5.1: The contours of $\mathrm{Im}[\omega_0 + \gamma\omega_1]$ in the k-β plane for the case $\theta_n = 0.06$, $F = 0.2$, $C_f = 0.01$, $M = 1$, $\gamma = 0$ (dashed line), $\gamma = 0.04$ (red dashed dotted line) and $\gamma = 0.1$ (solid thick line) for different lateral wavenumbers n. All the curve shown in this figure is neutral instability curves.

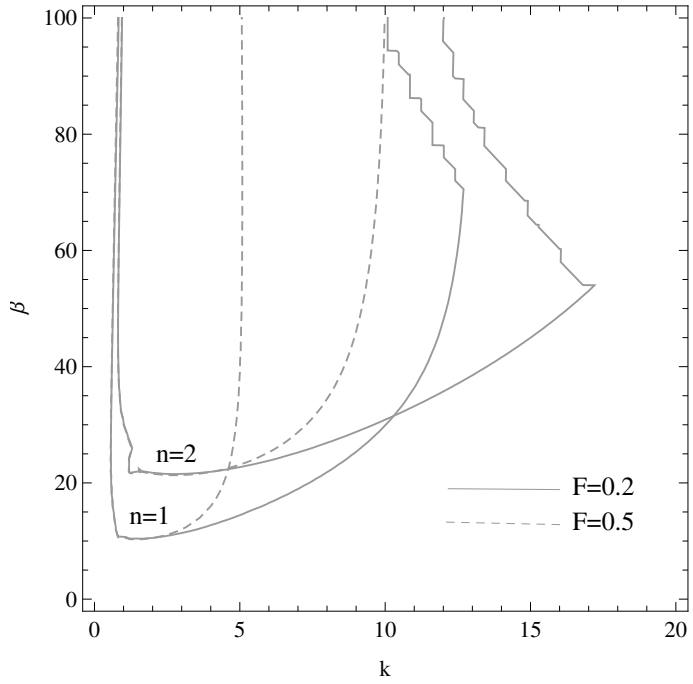

Figure 5.2: The contours of $\mathrm{Im}[\omega_0 + \gamma\omega_1]$ in the k-β plane for the case $\theta_n = 0.06$, $C_f = 0.01$, $M = 1$ and $\gamma = 0.1$for different values of Froude number F. All the curve shown in this figure is neutral instability curves.

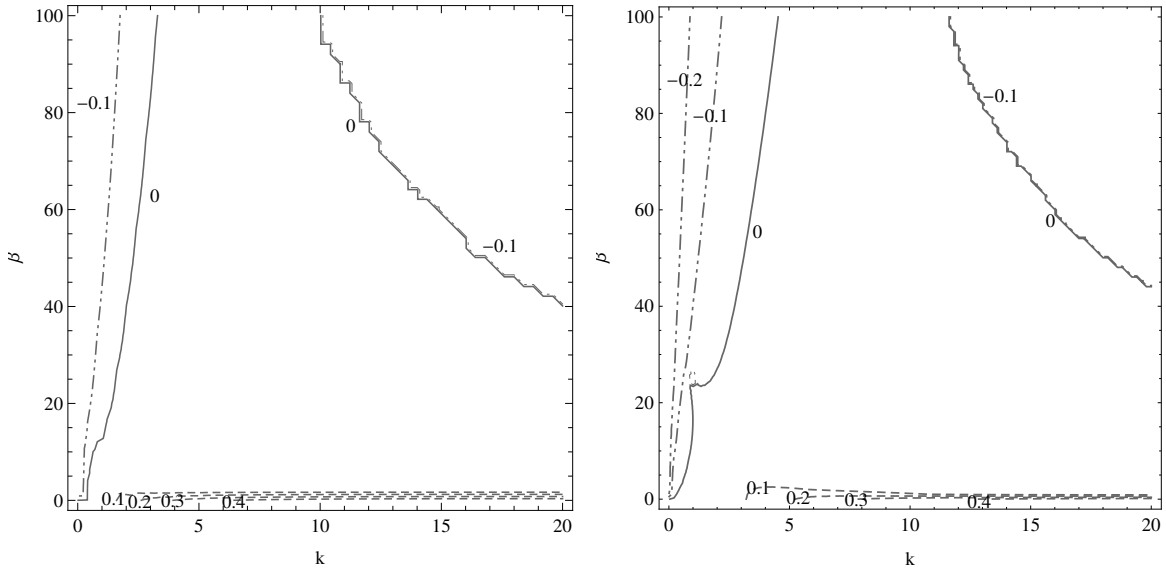

(a) $n = 1$ (Single alternate bars)

(b) $n = 2$ (Double row bars)

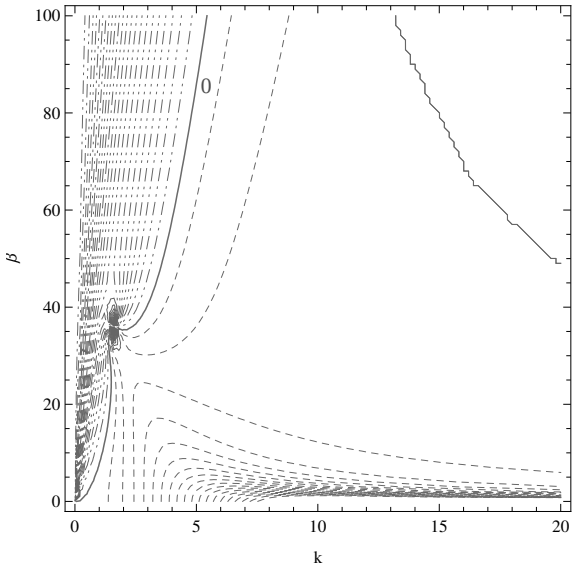

(c) $n = 3$ (Multiple bars)

Figure 5.3: The contours of $\mathrm{Im}[\omega_1]$ in the k-β plane for the case $\theta_n = 0.06$, $F = 0.2$, $C_f = 0.01$ and $M = 1$, where, solid lines indicate the neutral curve, and dotted lines and dashed dotted lines indicate the positive and negative contours of ω_1 respectively.

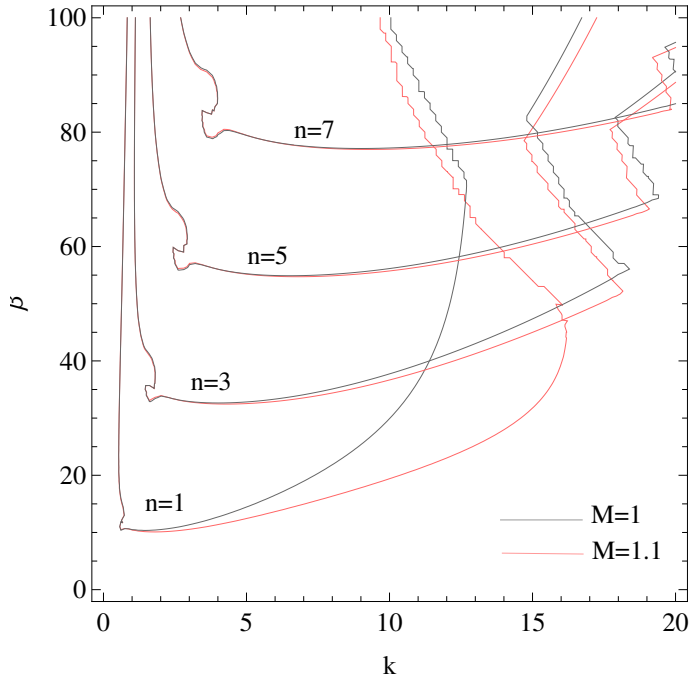

(a) Case of both banks being in phase

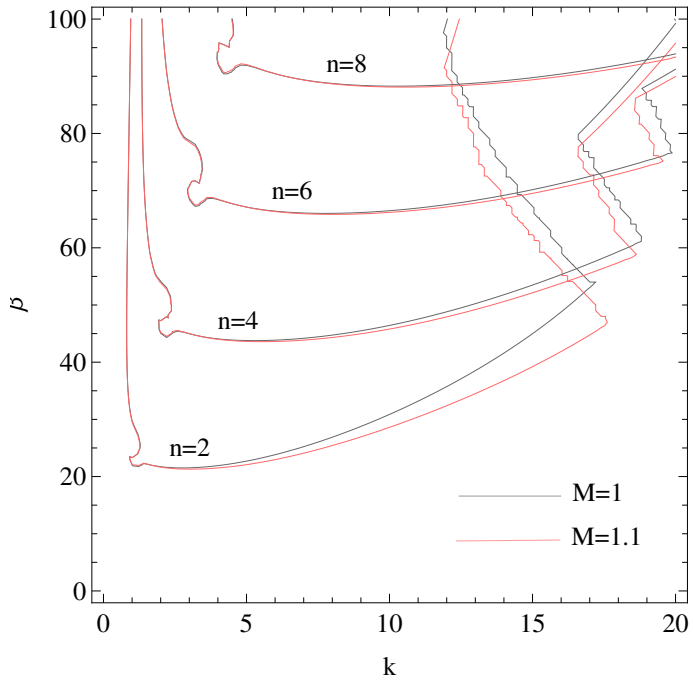

(b) Case of both banks being out of phase

Figure 5.4: The contours of $\mathrm{Im}[\omega_0 + \gamma\omega_1]$ in the k-β plane for the case $\theta_n = 0.06$, $F = 0.2$, $C_f = 0.01$, $\gamma = 0.1$, $M = 1$ (solid thick line) and $M = 1.1$ (red thick line) for different lateral wavenumbers n. All the curve shown in this figure is neutral instability curves.

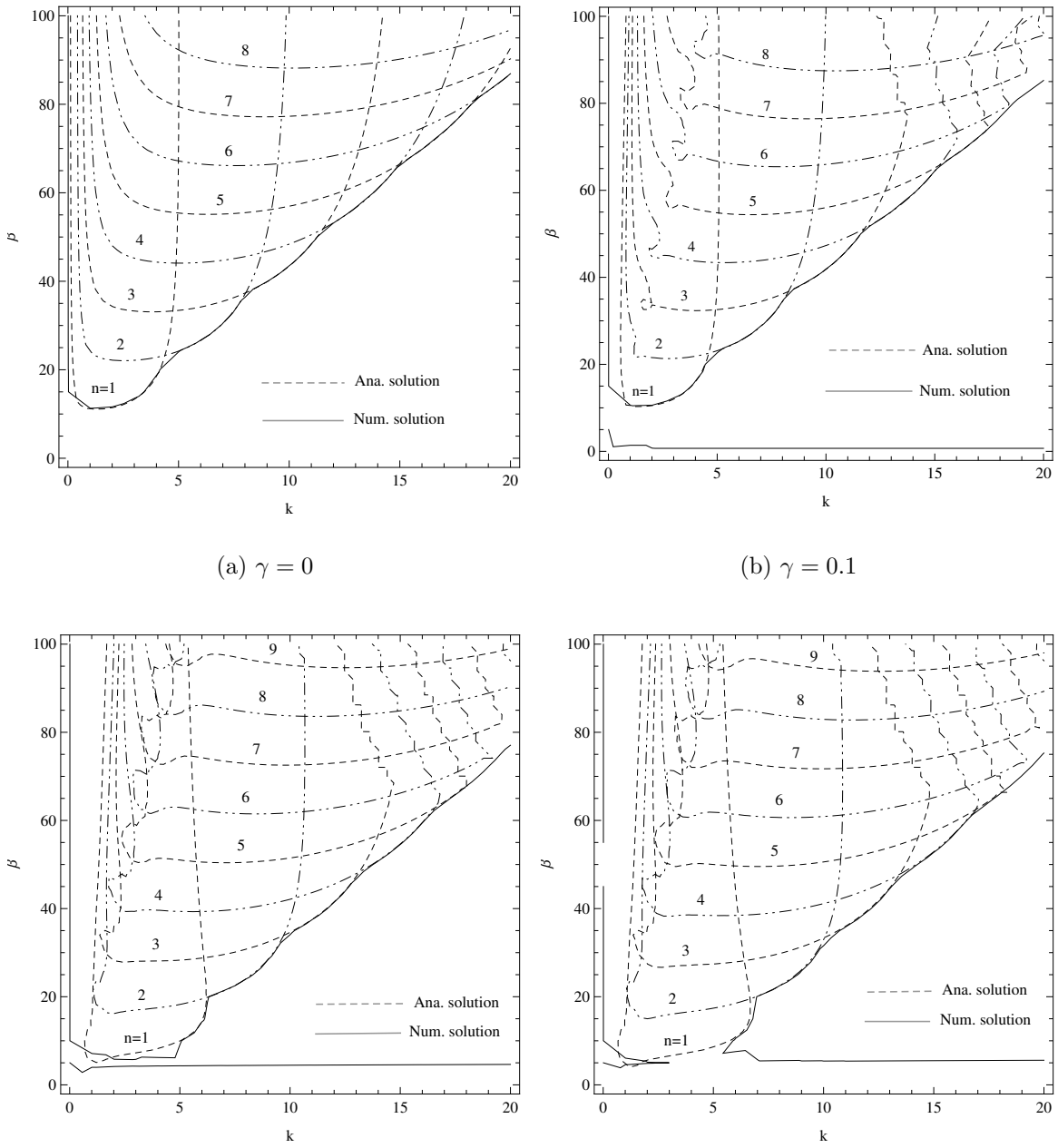

(a) $\gamma = 0$

(b) $\gamma = 0.1$

(c) $\gamma = 0.6$

(d) $\gamma = 0.7$

Figure 5.5: The contours of Im[ω] in the k-β plane for the case $\theta_n = 0.06$, $F = 0.5$, $C_f = 0.01$, and $M = 1$, where, the analytical solution is shown by the broken lines, and the numerical solution by the solid line. All the curve shown in this figure is neutral instability curves.

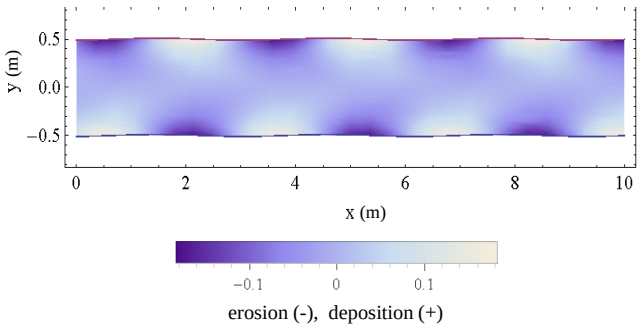

(a) bed level for $n = 1$ (present study)

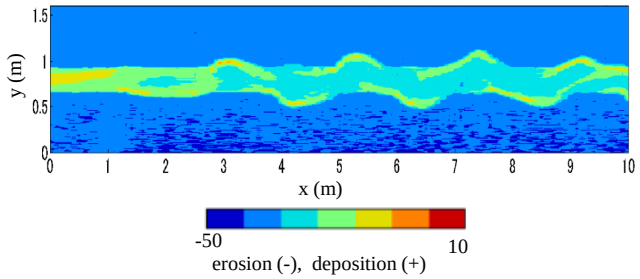

(b) bed level for channel width 0.25m (Watanabe's experiment)

Figure 5.6: (a) bed level for $n = 1$ (present study) and (b) bed level (Watanabe's experiment), where $\theta_n = 0.056$, $\theta_c = 0.034$, $F = 1.05$, $C_f = 0.009$, $M = 1$ and $\gamma = 0.5$. Flow directions from left to right.

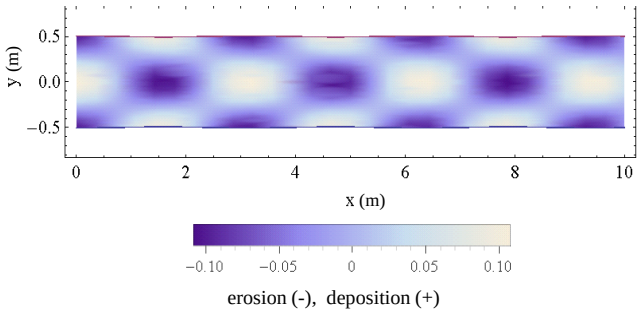

(a) bed level for $n = 2$ (present study)

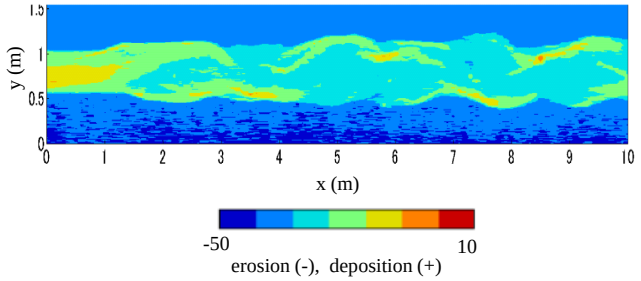

(b) bed level for channel width 0.45m (Watanabe's experiment)

Figure 5.7: (a) bed level for $n = 2$ (present study) and (b) bed level (Watanabe's experiment), where $\theta_n = 0.056$, $\theta_c = 0.034$, $F = 1.05$, $C_f = 0.009$, $M = 1$ and $\gamma = 0.5$. Flow directions from left to right.

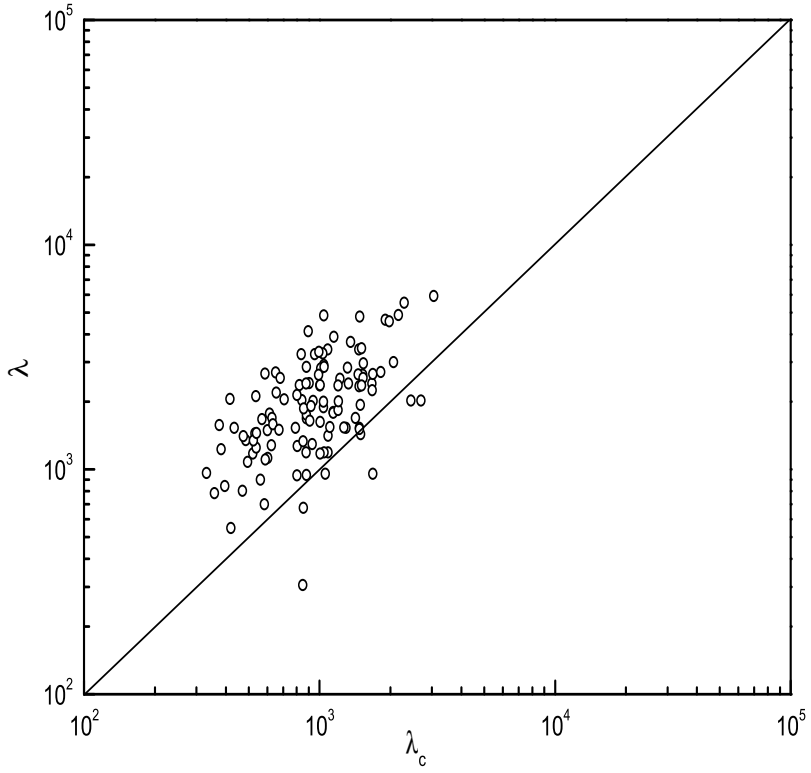

Figure 5.8: Test of our analysis with field data, where λ is the observed and λ_c is the predicted wavelength; the units are in meters. γ=4.27×10^{-5} to 4.39×10^{-2}.

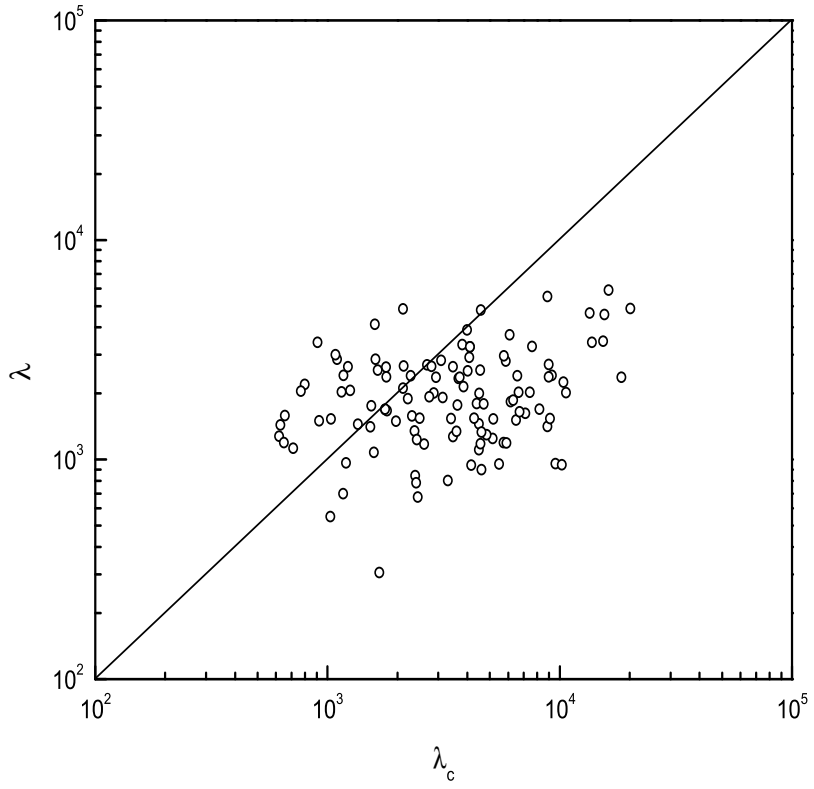

Figure 5.9: Test of meandering analysis performed by Ikeda et al. (1981) with field data, where λ is the observed and λ_c is the predicted wavelength; the units are in meters.

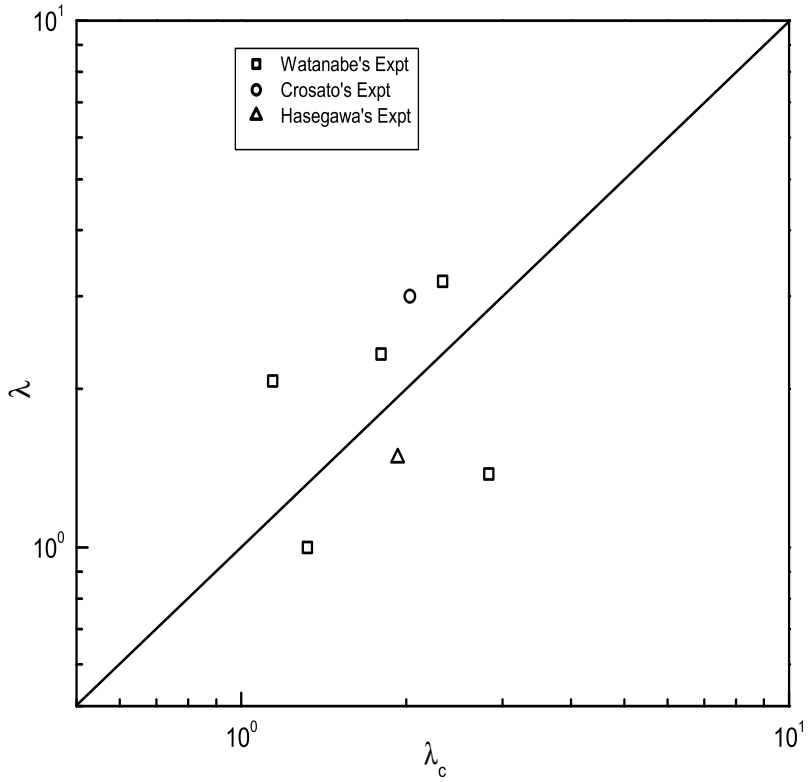

Figure 5.10: Test of our analysis with the experimental data obtained by Watanabe, Corasato and Hasegawa, where λ is the observed and λ_c is the predicted wavelength; the units are in meters. γ=0.5.

Chapter 6

Conclusion

A linear stability analysis of fluvial sand bars relating bank erosion was proposed. The analysis was performed by the use of the shallow water equations, the Exner equation, and the bank erosion equation newly proposed in this study. We make use of simple assumptions that the average value of total channel width kept constant, and the bank erosion takes place due to increases in the bed shear stress in the vicinity of banks, and the bank erosion speed depends on how large the bed shear stress at the junction is compared with the critical bed shear stress. The quasi-steady assumption has been employed in which time scale of flow variation is sufficiently short compared with that of topographical variations of bed and banks.

A perturbation technique has been used to analyze the shallow water equations in the linear stability analysis. The resulting perturbation equations are solved by numerically and analytically to see the comparison between them. The instability diagram obtained from numerical solution shows the contours of the maximum growth rate corresponding to multiple bars with a variety of lateral wavenumbers as well as single alternate bars. The instability diagram of fluvial bars without bank erosion and with bank erosion shows that the unstable region expands slightly in the range of large wavenumbers as the bank erosion coefficient increases. It can also be seen that the bed becomes unstable in a wider range of wavenumbers if the bank is more erodible. There was a tendency of increasing bed instability due to bank erosion.

In the analytical solution in order to obtain the solution up to $O(\gamma)$, the γ expansion has been used into the governing equations. Two simple cases of phase

shift has been specified between the right and left banks, one is the case of the both banks being in phase, and other is the case of the both banks being out of phase, which are commonly observed in the field. We have evaluated γ from field and experimental data to see effects of bank erosion on bar instability.

We obtained instability diagram from the analytical solution, and found that, the unstable regions located inside the areas surrounded by the neutral curves generally expands in the direction of increasing wavenumbers due to bank erosion. That tendency is remarkable especially in the case of single alternate bars. The expansion of unstable region in the direction of increasing wavenumber means that the wave length of bars decreases. Therefore, bank erosion has an effect to decrease the wavelength of bars. It is also found from the analysis that the bed is stabilized in the ranges of small wavenumbers, and of large wavenumbers and large aspect ratios due to bank erosion. We also found the discontinuous changes of neutral curves in the ranges of large aspect ratios and large wavenumbers. The discontinuity is not observed in the case of large Froude numbers, and it is suspected that the term at $O(\gamma)$ becomes too large for the expansion to be valid. The analytical solution in our analysis is assumed to be applicable only in the ranges of relatively small aspect ratios and small wavenumbers, and large Froude numbers.

The instability diagram obtained from the analytical solution and numerical solution shows that the envelope of all the neutral curves of analytical solution agrees well with the neutral curve of numerical solution in the range of large wavenumbers, and however, the agreement is not good in the range of small wavenumbers.

We have compared the bed topography obtained from our analysis with that obtained in the Watanabe's experiments (2015), and the similar pattern of bed topography has been found. We have also compared the wavelength of bars predicted by our analysis with field data, and found that the prediction obtained in our analysis agree better with the field data than that obtained in the analysis of meandering performed by Ikeda et al. (1981). This implies that the some cases of meandering can possibly be explained by our theory of the bar instability with bank erosion. Our analysis has been tested with the use of experimental data obtained by Watanabe, Corasato and Hasegawa, and seen a reasonable agreement between the prediction and the experimental data.

Bibliography

Beck, S. (1984). Mathematical modelling of meander interaction. In: *River Meandering*. ASCE. pp. 932–941.

Callander, R. A. (1969). Instability and river channels.. *J. Fluid Mech.* **36**, 465–480.

Chien, N. (1954). The present status of research on sediment transport. *J. Hydraul.Div., ASCE*.

Colombini, M., G. Seminara and Tubino M. (1987). Finite-amplitude alternate bars. *J. Fluid Mech.* **181**, 213–232.

Crosato, A. and E. Mosselman (2009). Simple physics-based predictor for the number of river bars and the transition between meandering and braiding. *Water Resources Research*.

Engelund, F. (1981). The motion of sediment particles on an inclined bed. *Progress Rep* **53**, 15–20.

Engelund, F. and E. Hansen (1967). *A Monograph on Sediment Transport in Alluvial Streams*. Copenhagen : Danish Technical Press.

Fu-Chun, Wu and Yeh Tzu-Hao (2005). Forced bars induced by variations of channel width: Implications for incipient bifurcation. *Journal of Geophysical Research: Earth Surface (2003–2012)*.

Fujita, Y. and Y. Muramoto (1985). Studies on the process of development of alternate bars. *Bulletin of the Disaster Prevention Research Institute* **35**(3), 55–86.

Hasegawa, K. (1989). Universal bank erosion coefficient for meandering rivers. *Journal of Hydraulic Engineering* **115**(6), 744–765.

Ikeda, S. and N. Izumi (1990). Width and depth of self-formed straight gravel rivers with bank vegetation. *Water Resources Research* **26**(10), 2353–2364.

Ikeda, S., G. Parker and K. Sawai (1981). Bend theory of river meanders. part 1. linear development. *J. Fluid Mech.* **112**, 363–377.

Johannesson, H. and G. Parker (1985). Computer simulated migration of meandering rivers in minnesota.

Keulegan, G. H. (1938). *Laws of turbulent flow in open channels*. Vol. 21. National Bureau of Standards US.

Olesen, K. W. (1983). Alternate bars in and meandering of alluvial rivers. Technical report. Delft University of Technology.

Parker, G. (1978b). Self-formed straight rivers with equilibrium banks and mobile bed. part 2. the gravel river. *J. Fluid Mech.* **89(1)**, 127–146.

Parker, G. (1982). Stability of the channel of the minnesota river near state bridge no. 93, minnesota.

Seminara, G. and M. Tubino (1989). Alternate bars and meandering: Free, forced and mixed. *River meandering, Water Resourc. Monogr. Ser.* **12**, 267–320.

AppendixA

Notation

The following symbols are used in this paper:

A = amplitude of perturbation (-);

$\mathcal{A}$ = coefficient defined in equation (4.7)(-);

B = dimensionless channel width (-);

$\tilde{B}$ = channel width (m);

$\tilde{B}_n$ = channel width in the base state flat bed condition (m);

$\mathcal{B}$ = coefficient defined in equation (4.7)(-);

C_f = bed friction coefficient (-);

$\mathcal{C}$ = coefficient defined in equation (4.7)(-);

d_s = dimensionless sediment diameter (-);

$\tilde{d}_s$ = sediment diameter (mm);

E_0 = Hasegawa's bank erosion coefficient (-);

$(\boldsymbol{e}_{NL}, \boldsymbol{e}_{NR})$ = dimensionless unit vectors normal to the left and right banks (-);

F = Froude number (-);

g = gravitational acceleration (ms^{-2});

H = dimensionless flow depth (-);

$\tilde{H}_n$ = flow depth in the base state flat bed condition (m);

k = dimensionless wavenumber of perturbation (-);

k_s = roughness height (m);

k_{max} = wavenumber at which instability is maximized(-);

L = location of the left bank (-);

$\tilde{L}$ = location of the left bank (m);

$\mathsf{L}(\alpha)$ = parameter defined in equation (4.2)(-);

M = dimensionless bank height (-);

$\tilde{M}$ = bank height (m);

n = lateral wavenumber (-);

Q_b = dimensionless total bedload rate (-);

$\tilde{Q_b}$ = total bedload rate (m^3s^{-1});

Q_{bx} = x component of dimensionless bedload sediment rate (-);

Q_{by} = y component of dimensionless bedload sediment rate (-);

$\tilde{Q_{bx}}$ = $\tilde{x}$ component of bedload sediment rate (m^3s^{-1});

$\tilde{Q_{by}}$ = $\tilde{y}$ component of bedload sediment rate (m^3s^{-1});

$\boldsymbol{Q}_b$ = dimensionless bedload vector (-);

r = constant (-);

R = location of the right bank (dimensionless) (-);

$\tilde{R}$ = location of the right bank (m);

R_s = submerged specific gravity (-);

$\boldsymbol{r}(\alpha)$ = parameter defined in equation (4.2) (-);

S = longitudinal bed slope (-);

t = dimensionless time (-);

$\tilde{t}$ = time (s);

$\tilde{T_b}$ = total bed shear stress (Pa);

$T_j(\xi)$ = Chebyshev polynomials in ξ of degree j(-);

$\tilde{U_n}$ = flow velocity in the base state flat bed condition (ms^{-1});

U = x component of dimensionless flow velocity (-);

V = y component of dimensionless flow velocity (-);

$\tilde{U}$ = $\tilde{x}$ component of flow velocity (ms^{-1});

$\tilde{V}$ = $\tilde{y}$ component of flow velocity (ms^{-1});

$\boldsymbol{U}$ = dimensionless velocity vector (-);

u_B = excess of near-bank depth-averaged stream-wise flow velocity (ms^{-1});

x = dimensionless streamwise direction (-);

y = dimensionless lateral direction (-);

$\tilde{x}$ = streamwise direction (m);

$\tilde{y}$ = lateral direction (m);

Z = dimensionless bed elevation (-);

$\tilde{Z}$ = bed elevation (m);

β = aspect ratio (-);

γ = dimensionless bank erosion coefficient (-);

$\tilde{\gamma}$ = dimensional version of the bank erosion coefficient (ms^{-2});

θ = non-dimensional bed shear stress (-);

θ_c = non-dimensional critical bed shear stress (-);

θ_n = non-dimensional bed shear stress in the base state flat bed condition (-);

ϕ = angle between the direction of bed load and x axis (-);

ψ = angle between the bank and the axis (-);

ρ = density of water (kgm^{-3});

$\tilde{\zeta}$ = bank erosion rate (ms^{-1});

λ = observed wavelength (m);

λ_p = porosity (-);

λ_c = wavelength corresponding k_{max} (m); and

ω = dimensionless complex angular frequency of perturbation (-);

AppendixB

Table 6.1: Field data has been used to calculate the values of γ and λ_c. In this table $\tilde{B_n}$=channel width (m), $\tilde{H_n}$=flow depth (m), $\tilde{d_s}$=sediment diameter (mm), γ=bank erosion coefficient, λ=observed wavelength (m), and $\lambda_{c(our)}$ and $\lambda_{c(ikeda)}$=predicted wavelength (m) of our's and ikeda's analysis respectively.

Rivers	Bars	$\tilde{B_n}$	$\tilde{H_n}$	$\tilde{d_s}$	θ_n	γ	λ	$\lambda_{c(our)}$	$\lambda_{c(ikeda)}$
Saru	double	582	1.54	8.70	0.117	1.3E-03	2640	1524	1788
	single	280	1.84	18.90	0.064	7.5E-04	1692	880	1770
	single	281	2.10	16.20	0.135	4.5E-04	1896	1039	2216
	double	331	1.54	31.10	0.055	4.2E-04	2422	904	1170
Tokachi	double	308	1.73	22.20	0.060	6.3E-04	1756	880	1544
	double	275	1.35	26.60	0.065	4.4E-04	1530	789	1035
Mogami M	single	225	5.18	34.56	0.052	3.8E-04	1194	1087	5718
Mogami D	single	327	3.94	25.50	0.058	5.3E-04	1804	1141	4390
	double	330	4.43	24.60	0.074	4.4E-04	1534	1296	5171
	single	218	4.21	26.90	0.180	1.6E-04	1792	1141	4710
Abukuma	single	235	3.50	19.50	0.138	3.3E-04	2920	1040	4081
Omono U	single	214	4.30	14.00	0.144	5.2E-04	2812	1011	5854
Yoneshiro	single	312	5.70	15.35	0.083	7.9E-04	1696	1421	8173
	single	190	6.30	18.37	0.129	3.9E-04	1414	1085	8841
	single	208	5.00	26.88	0.100	2.8E-04	1192	1046	5893
Watarase	single	301	1.64	40.90	0.064	2.3E-04	2036	841	1150

	double	203	1.62	93.40	0.066	6.6E-05	2200	654	798
	double	199	1.41	103.50	0.061	6.2E-05	1280	625	619
Fuefuki	single	69	2.30	5.50	0.226	1.4E-03	1536	434	3405
Agano	double	815	2.90	1.10	0.107	3.2E-02	2026	2438	6653
	double	815	3.60	2.20	0.268	4.5E-03	2026	2695	7438
	single	284	4.00	55.80	0.051	1.9E-04	2644	991	3470
Shinano	single	445	2.04	2.30	0.240	4.7E-03	2346	1472	3654
Chikuma	double	387	2.60	13.70	0.113	6.9E-04	2836	1314	3083
	single	166	2.20	22.30	0.057	6.6E-04	2668	586	2126
	double	280	2.00	34.60	0.079	2.5E-04	2864	880	1607
	double	303	1.60	42.10	0.114	1.3E-04	2868	1046	1099
Kurobe	braided	302	1.80	99.00	0.094	4.3E-05	3428	1084	906
Kano	single	116	2.50	20.00	0.087	5.1E-04	1176	521	2608
	single	131	2.00	55.10	0.116	8.3E-05	1448	531	1349
Yahagi	double	280	2.00	1.43	0.390	5.9E-03	3900	1150	3988
	single	232	3.10	1.71	0.857	2.1E-03	2412	1325	6554
	single	267	3.00	1.91	0.167	9.0E-03	1840	1198	6142
	single	198	2.60	3.38	0.844	7.5E-04	2000	1037	4498
Kiso D	single	632	5.30	0.47	1.456	8.4E-03	5924	3055	16227
Nagara	single	189	5.24	13.60	0.156	5.0E-04	3282	1033	7589
	single	235	4.27	44.00	0.072	1.9E-04	3260	953	4104
Kizu D	single	342	3.61	6.56	0.280	8.4E-04	2974	1535	5741
Ina	single	114	2.28	12.38	0.295	3.1E-04	2704	651	2679
Mo	single	128	2.03	16.28	0.101	6.0E-04	2118	536	2116
Kino	single	353	3.98	23.22	0.181	2.0E-04	4796	1479	4577
Yamato	single	144	3.45	2.15	0.832	1.5E-03	1626	1005	7097
	single	109	2.88	1.37	1.208	2.0E-03	1868	856	6291
	single	117	2.88	12.43	0.130	6.9E-04	1774	613	3620
	single	89	1.79	6.44	0.315	7.7E-04	1352	486	2370
Kako	single	306	2.68	19.90	0.180	2.5E-04	2012	1202	2862
	single	98	4.26	30.60	0.136	1.7E-04	902	560	4596

	single	160	3.40	29.30	0.151	1.6E-04	1272	804	3463
Kuzuryu	double	331	2.86	62.40	0.064	1.3E-04	4860	1040	2110
	single	94	4.47	26.15	0.076	3.9E-04	1250	537	5136
	single	103	4.31	34.91	0.118	1.6E-04	1108	588	4478
Ibo	double	145	2.28	41.40	0.079	1.9E-04	1674	569	1801
	single	117	2.45	81.80	0.076	7.0E-05	1410	474	1530
	double	85	2.56	28.90	0.067	3.8E-04	844	396	2387
	double	195	2.16	43.40	0.075	1.8E-04	2556	681	1644
	single	148	2.72	62.20	0.091	8.8E-05	1496	600	1971
	single	106	2.09	76.90	0.070	8.4E-05	2064	416	1253
Shigenobu	single	170	1.90	21.50	0.100	4.0E-04	1698	628	1770
	double	251	0.96	26.30	0.118	2.5E-04	1194	876	649
	braided	309	0.95	27.70	0.190	1.4E-04	1436	1493	626
	double	278	1.53	26.90	0.341	8.3E-05	2650	1456	1223
Gogase	single	231	3.33	21.64	0.143	2.7E-04	2370	1001	3706
	single	87	1.42	21.35	0.068	5.9E-04	966	331	1200
Shira	single	74	1.82	7.61	0.103	1.8E-03	1580	375	2309
	single	75	1.93	1.85	0.714	2.2E-03	1344	524	3594
	single	122	1.47	10.60	0.140	8.2E-04	1080	495	1584
Kushiro		57	1.85	7.12	0.202	1.0E-03	784	358	2403
Saru		248	1.94	22.60	0.095	3.9E-04	2378	820	1790
Tokachi		262	1.54	2.62	0.866	1.1E-03	1542	1266	2491
		232	0.98	27.60	0.065	4.2E-04	1590	634	655
Mogami U		194	3.88	36.40	0.051	3.5E-04	2148	802	3845
Mogami D		388	3.26	4.75	0.462	8.3E-04	956	1681	5483
Omono U		272	2.28	20.80	0.078	5.4E-04	2412	876	2280
		269	2.89	10.68	0.067	1.7E-03	3340	994	3797
		332	5.40	7.32	0.215	9.3E-04	2416	1669	9246
		282	6.70	22.17	0.139	2.7E-04	1536	1477	9080
Tone U		302	3.89	0.17	2.967	1.8E-02	4644	1898	13465
		473	2.59	0.13	5.249	1.7E-02	5532	2286	8847

Tone D		344	5.60	0.20	0.983	4.4E-02	4874	2161	20099
		252	4.44	0.37	0.868	2.0E-02	3428	1466	13757
		346	4.86	0.34	1.043	1.9E-02	4572	1976	15573
		192	5.26	0.60	0.788	1.1E-02	3466	1508	15349
Watarase		239	1.55	88.20	0.060	8.0E-05	2050	708	768
Kamanashi		173	3.24	9.36	0.438	3.1E-04	1180	1006	4558
		308	1.63	2.39	1.033	1.0E-03	1936	1489	2737
		426	1.07	9.40	0.384	3.6E-04	3000	2059	1083
Agano		438	4.00	24.40	0.061	5.4E-04	2554	1529	4538
		565	1.30	0.66	0.670	1.1E-02	2662	1682	2799
Shinano		369	2.40	3.60	0.104	5.5E-03	2534	1220	4007
Tedori		296	2.20	50.00	0.075	1.5E-04	4126	894	1598
		97	3.20	0.18	3.933	1.3E-02	2022	938	10640
		128	2.60	0.12	5.646	1.7E-02	2380	1005	8951
Nagara		193	4.27	44.00	0.054	2.5E-04	3260	836	4104
Yasu		86	3.16	8.80	0.279	5.4E-04	1456	540	4490
		84	2.97	0.20	23.760	1.9E-03	958	1056	9562
Katsura		84	3.74	0.61	6.375	1.3E-03	946	880	10203
		143	3.33	14.71	0.204	3.4E-04	944	802	4158
		163	3.65	13.01	0.614	1.4E-04	1296	931	4845
Kino		405	5.99	13.74	0.080	9.7E-04	2716	1818	8966
		205	3.09	26.97	0.144	2.0E-04	1920	920	3135
Yamato		253	2.29	2.17	0.330	3.7E-03	1544	1104	4276
Kuzuryu		253	4.32	1.33	1.805	1.4E-03	2254	1673	10357
		139	6.14	0.61	11.347	7.3E-04	2370	1506	18406
		331	4.13	7.90	0.204	8.7E-04	1512	1475	6482
		149	4.59	41.73	0.161	9.1E-05	1336	851	4596
Ibo		82	2.41	21.65	0.070	5.6E-04	1232	382	2422
Hino		270	1.64	14.07	0.105	7.1E-04	306	848	1673
		117	2.04	112.13	0.063	5.3E-05	550	420	1027
Tenjin		217	2.09	11.56	0.164	6.1E-04	676	852	2442

		150	1.45	25.00	0.141	2.2E-04	700	582	1167
Gouno		280	5.90	49.00	0.131	8.8E-05	3700	1353	6081
Umaarai		324	3.26	41.00	0.110	1.4E-04	2370	1198	2930
		159	5.07	18.20	0.182	2.8E-04	1650	908	6716
Shigenobu		198	1.20	23.70	0.111	3.1E-04	1504	672	919